frontiers | Frontiers in Nanotechnology

TYPE Original Research
PUBLISHED 19 September 2025
DOI 10.3389/fnano.2025.1634210

OPEN ACCESS

EDITED BY
Benedetta Marmiroli,
Graz University of Technology, Austria

REVIEWED BY
Sumea Klokic,
Graz University of Technology, Austria
Andrea Veronica Bordoni,
National Atomic Energy Commission, Argentina

*CORRESPONDENCE
Alessandra Pinna,
a.pinna@surrey.ac.uk

RECEIVED 23 May 2025
ACCEPTED 29 August 2025
PUBLISHED 19 September 2025

CITATION
Palomeque Chávez JC, Mohammed AA, Aghajanpour S, Li S, Enzo S, Kelly NL, Bradley DG, Kerherve G, Porter AE, Hanna JV, Jones JR and Pinna A (2025) One-pot sol–gel synthesis of Sr/Ca-doped silica nanoparticles for osteogenic therapy in osteoporosis. *Front. Nanotechnol.* 7:1634210. doi: 10.3389/fnano.2025.1634210

One-pot sol–gel synthesis of Sr/Ca-doped silica nanoparticles for osteogenic therapy in osteoporosis

Juan C. Palomeque Chávez[1], Ali A. Mohammed[2], Sareh Aghajanpour[3], Siwei Li[1,4], Stefano Enzo[5], Nicole L. Kelly[6], David G. Bradley[6], Gwilherm Kerherve[1], Alexandra E. Porter[1], John V. Hanna[6,7], Julian R. Jones[1] and Alessandra Pinna[1,3]*

[1]Department of Materials, Imperial College London, London, United Kingdom, [2]Dyson School of Design Engineering, Imperial College London, London, United Kingdom, [3]School of Veterinary Medicine, Faculty of Health and Medical Sciences, University of Surrey, Guildford, United Kingdom, [4]Visiting Specialist Services Academy Ltd, London, United Kingdom, [5]Department of Chemistry and Pharmacy, University of Sassari, Sassari, Italy, [6]Department of Physics, University of Warwick, Coventry, United Kingdom, [7]School of Material Science and Engineering, Nanyang Technological University, Singapore, Singapore

Osteoporosis affects more than 200 million people worldwide, with an osteoporotic fracture occurring approximately every 3 seconds; with ageing populations, its prevalence continues to rise, yet it remains under-diagnosed and under-treated. Strontium- and calcium-doped mesoporous bioactive glass nanoparticles (BGNPs) are promising due to their ability to combine bioactive bone-regenerative function with controlled therapeutic ion release. We optimized a one-step sol–gel (modified Stöber) synthesis by varying the solvent system (pure water vs. 1:1 ethanol/water) to control BGNP size and morphology and assessed their effects on pre-osteoblasts (MC3T3-E1). Characterization by electron microscopy, X-ray photoelectron spectroscopy, and ˆ29Si MAS NMR showed that ethanol inclusion yielded smaller, uniform spherical particles (74 ± 5 nm), whereas water alone produced significantly larger particles (224 ± 42 nm). Both Sr^{2+} and Ca^{2+} were incorporated as network modifiers within an amorphous silicate framework, with no crystalline phases. Cytocompatibility assays revealed a size-dependent response: larger particles reduced cell viability at 1 μg/mL, while both sizes were biocompatible at 0.1 μg/mL. At the non-toxic concentration of 0.1 μg/mL, BGNPs enhanced alkaline phosphatase activity, promoted osteogenic differentiation, and exhibited antioxidant activity by scavenging tert-butyl hydroperoxide-induced free radicals. These results indicate that solvent-controlled synthesis effectively tunes BGNP size without disrupting silicate network integrity, and that properly sized Sr/Ca-doped BGNPs support both osteogenic and antioxidant responses, making them strong candidates for advanced therapeutic approaches in osteoporosis treatment.

KEYWORDS

silica mesoporous nanoparticles, osteoporosis, sol-gel method, radical scavenger, therapeutic ions

Introduction

Currently, osteoporosis affects more than 200 million people worldwide (Al Zadjali et al., 2024), and an osteoporotic fracture occurs approximately every 3 seconds (Ou et al., 2025). With global population ageing, the prevalence continues to rise. Despite its substantial clinical burden, osteoporosis remains frequently under-diagnosed and under-treated. Many individuals only become aware of their condition after sustaining a low-trauma fracture that requires hospitalization (Chandran et al., 2024; Fuggle et al., 2024). Pathologically, osteoporosis involves a loss of bone mass and disruption of normal skeletal architecture, leaving bone fragile and prone to fracture (Tu et al., 2018; Ghahri et al., 2023). The underlying cause is an imbalance in bone remodelling: osteoclast resorption exceeds osteoblast matrix deposition, which enlarges pore volume and weakens the tissue (Al Zadjali et al., 2024). Post-menopausal women are especially susceptible, because the decline in oestrogen levels lifts its inhibition of osteoclasts while also reducing osteoblast activity, thereby accelerating bone loss (Fischer and Haffner-Luntzer, 2022). Epidemiological data indicate that about 40% of women develop osteoporosis after menopause (Yao et al., 2025).

Adequate calcium (Ca^{2+}), phosphate, and vitamin D, along with exercise and healthy lifestyle choices, are key to osteoporosis prevention and could avoid up to nine million fractures annually (Diba et al., 2017; Tu et al., 2018). High-dose Ca^{2+} supplements may increase kidney stone risk, unlike dietary sources. Current osteoporosis treatments predominantly rely on anti-resorptive agents. Bisphosphonates, which inhibit osteoclast-mediated bone resorption, are effective in slowing further bone loss but do not restore existing skeletal defects (Kim et al., 2017). Prolonged use of bisphosphonates has been associated with adverse outcomes such as over suppression of bone remodelling, atypical fractures, and osteonecrosis of the jaw (Jelin-Uhlig et al., 2024). In contrast, anabolic approaches such as recombinant human parathyroid hormone (rhPTH 1-34) and abaloparatide aim to enhance osteoblast activity, promoting bone formation to meet or exceed resorption rates. Efficacy is typically assessed by upregulation of osteogenic markers, including RUNX2, alkaline phosphatase (ALP), osteopontin (OPN), osteocalcin (OCN), bone morphogenetic protein-2 (BMP2), and type I collagen (Aghajanpour et al., 2022; Celik et al., 2024). Agents such as rhPTH 1-34 and estradiol (E2) have demonstrated the ability to increase these markers in preclinical models; however, chronic systemic administration poses risks of significant side effects (Xuan et al., 2025; Sakurai et al., 2024). Therefore, there is growing interest in developing targeted delivery systems that enable sustained, localised release of osteogenic stimuli while minimizing systemic toxicity.

Bioactive glasses have been researched extensively in tissue engineering and drug delivery (Naruphontjirakul et al., 2022). Due to their osteogenic and biodegradable nature attributed to release of ions to promote osteogenesis, they have been used across a range of biomedical fields, including orthopaedics and dentistry (Gritsch et al., 2021; Meskher et al., 2024; Moghaddam et al., 2025). The original 45S5 Bioglass®, composed of 46.1 mol% SiO_2, 24.4 mol% Na_2O, 26.9 mol% CaO, and 2.6 mol% P_2O_5, showed that the osteogenic properties were attributed to soluble silica and Ca^{2+} ions during biodegradation (Siekkinen, 2024). More recently, focus has shifted towards bioactive glass nanoparticles (BGNPs) that have shown the potential for therapeutic drug delivery (Zhang et al., 2025) and promote differentiation of pre-osteoblasts (Jacobsen et al., 2025) due to their biomaterial properties such as large specific surface area and surface to volume ratio (García-Perdiguero et al., 2025). Core-shell BGNPs offer further advantages, including greater structural stability, shielding of encapsulated molecules from harsh environments, and tighter control over release rates. These features have broadened their use in drug-delivery systems, cell-biology studies, and biosensor platforms (Talib et al., 2025). For instance, Hembury et al. have demonstrated the advantages of using hollow mesoporous silica shell hosting AuQDs, which stabilise the otherwise water insoluble gold nanostructures, enabling the use of AuQDs in biological environments (Hembury et al., 2015).

BGNPs are silica-based nanostructures enriched with CaO, Na_2O and P_2O_5 which can be doped with various cations such as Sr^{2+}, Zn^{2+}, Mg^{2+}, Co^{2+} and Ag^{+} to give diverse functionalities such as promoting osteogenesis, angiogenesis, cell proliferation, reducing inflammation, and providing antibacterial effects (Lee et al., 2017). The incorporation of Si^{4+}, Ca^{2+}, and other ions within the structure enables strong bonding to bone tissue, while the ions released into the surrounding environment provide osteogenic signals that promote bone formation (Islam et al., 2017; Naruphontjirakul et al., 2018). Furthermore, substituting cations such as Ca^{2+} and Sr^{2+} into the SiO_2 framework disrupts its network structure, accelerating biodegradation when exposed to an aqueous environment (Islam et al., 2017).

Using BGNPs rather than bulk bioactive glass greatly enlarges the available surface area for functionalisation, accelerates ion release and, as a result, enhances biological activity (Hesaraki et al., 2021). Among the available fabrication methods, the modified sol-gel (Stöber) process remains particularly advantageous. It operates at near-ambient temperature, permits uniform incorporation of heat-sensitive therapeutic ions, and yields nanoparticles with high specific surface area and tunable mesoporosity properties essential for rapid ion dissolution and controlled drug delivery (Foroutan et al., 2024). The inclusion of ethanol as a co-solvent in the sol–gel process is known to influence key aspects of nanoparticle formation, particularly the hydrolysis and condensation kinetics of silica precursors such as TEOS. Ethanol reduces the dielectric constant and polarity of the solvent mixture compared to water, which slows the hydrolysis rate and allows for more controlled and uniform condensation. This typically yields smaller, more monodisperse particles, as demonstrated in modified Stöber synthesis studies (Saha et al., 2023; Brinker et al., 1990). An ethanol-to-water molar ratio should be selected based on its demonstrated ability to balance precursor solubility with controlled nanoparticle morphology (Pierre et al., 2005). In addition, ethanol influences ion incorporation; while it slightly lowers the solubility of calcium and strontium nitrate salts, it also moderates silica network formation, thereby enabling uniform integration of Ca^{2+} and Sr^{2+} ions into the amorphous matrix without inducing crystallinity.

Ca^{2+} and Sr^{2+} are among the most frequently employed ion substitutions in BGNPs for osteoporosis treatment. Due to their structural similarities, both ions expand the nanoparticle framework, thereby enhancing its degradability in aqueous environments (Naruphontjirakul et al., 2018). Ca^{2+} plays a crucial role in bone regeneration by promoting hydroxyapatite (HA) deposition, regulating osteogenic activity, and stimulating angiogenesis (Malhotra and Habibovic, 2016; Choe et al., 2022). Similarly, Sr^{2+} is considered a "bone-seeking" element because of its similarities with Ca^{2+} and its ability to upregulate osteogenic markers such as ALP, RUNX2, and OCN, while concurrently inhibiting osteoclast activity (Huang and Ding, 2025). Sr^{2+} increases osteoblast metabolic activity and suppresses osteoclast-mediated bone resorption. Furthermore, Sr^{2+} facilitates the differentiation and maturation of precursor cells into osteoblasts, promoting matrix mineralization. Consequently, both *in vitro* and *in vivo* studies have demonstrated that Sr^{2+} significantly alleviates osteoporosis symptoms and reduces fracture risk (You et al., 2022; Shishkina et al., 2023). These effects have been extensively investigated in ovariectomised rat models, where localized delivery of ions has been shown to promote bone tissue recovery (Aveline et al., 2021). However, the therapeutic efficacy of Sr^{2+} *in vivo* is dose-dependent: low concentrations support osteogenic differentiation and bone formation, whereas high doses exert detrimental effects (Kourkoumelis, 2016). Optimal Sr^{2+} concentrations for bone regeneration have been identified within the range of 2–6 $\mu g/mL^{-1}$ (Naruphontjirakul et al., 2018).

This study focused on the synthesis of spherical and core-shell-like BGNPs doped with Sr^{2+} and Ca^{2+} ions, using a one-pot modified Stöber process. The method utilised either pure water or a mixture of water and ethanol as solvents to explore how these different media influence the nanoparticles' size, morphology, and the behaviour of Ca^{2+} and Sr^{2+} ions within the silica network. BGNPs biological activity and their capacity to scavenge reactive oxygen species (ROS) were assessed by using a monoculture of pre-osteoblast MC3T3-E1 cells. These cellular assays provided insight into how variations in nanoparticle morphology and size impact cellular responses critical to bone regeneration. The compositions of the BGNPs were designed based on insights from prior research, which demonstrated that Sr^{2+} doping within the range of 3–11 mol% significantly enhances osteogenic markers such as ALP expression and mineralization (Naruphontjirakul et al., 2018). Building on these findings, this study sought to elucidate the relationship between BGNPs morphology and their interaction with osteoblasts, alongside evaluating how the incorporation of bioactive ions like Sr^{2+} and Ca^{2+} modulates osteogenic differentiation and the mitigation of oxidative stress through free radical scavenging, highlighting their therapeutic potential in the management and treatment of osteoporosis.

Materials and methods

Materials

Cetyltrimethylammonium bromide (CTAB ≥98%, Sigma-Aldrich), sodium hydroxide (NaOH 2M, Merck KGaA), t-butyl hydroperoxide (TBHP, Sigma-Aldrich), strontium nitrate ($Sr(NO_3)_2$, Sigma-Aldrich), calcium nitrate ($Ca(NO_3)_2$, Sigma-Aldrich), dimethyl sulfoxide (DMSO anhydrous, ≥99.9%; Sigma-Aldrich), ammonium hydroxide solution (NH_4OH, 28% NH_3 in H_2O, ≥99.99%, Sigma Aldrich), tetraethyl orthosilicate (TEOS 99%, ABCR GmbH), ethanol (EtOH 99.9%, VWR chemicals), distilled water, anhydrous lithium metaborate (BiO_2Li) (80% w/w), lithium tetraborate ($Li_2B_4O_7$) (20% w/w) (Alfa Aesar), 5 M aqueous ammonia (NH_4OH, Aldrich), were used, as received, without any further purification. Minimum Essential Medium (α-MEM, A10490 Gibco) was purchased from Life-Technologies. 10% fetal bovine serum (FBS), penicillin, streptomycin, 3-(4,5-Dimethyl-thiazol-2-yl)-2,5, diphenyltetrazolium bromide for the MTT assay were purchased from Thermo Fisher Scientific, Hemel Hempstead, UK. Murine, pre-osteoblastic MC3T3-E1 cells were provided by ATCC. DCFDA -Cellular Reactive Oxygen Species Detection Assay Kit was purchased by ab113851.

Synthesis

BGNPs were synthesised with two different morphologies, spherical (~75 nm diameter) and core-shell-like (~220 nm diameter), using a one-pot modified Stöber method (Pinna et al., 2021). The morphology of the BGNPs was determined by the type of solvent used; pure water for the core-shell-like BGNPs and a mixture of ethanol/water for the smaller spherical BGNPs. In each case, 0.58 g of CTAB, 2.14 g of $Ca(NO_3)_2$, 1.92 g of $Sr(NO_3)_2$ and 400 μL of NH_4OH were dissolved in a 46.81 mL of solvent, either DI water for core-shell-like particles or a mixture of 23.41 mL DI water and 23.41 mL ethanol for the spherical particles (corresponding to a 0.3:1 M ratio of ethanol/water). Soon after, 2.72 mL of TEOS was added to the solution and stirred overnight at 450 rpm at room temperature. Shortly afterward, the BGNPs were washed using a centrifuge-based procedure. The solutions were transferred to 50 mL falcon tubes and centrifuged at 7,830 rpm for 40 min. After decanting the supernatant, the pellets were resuspended in ethanol and sonicated for 10 min. The process of centrifugation and washing was repeated twice more using water as solvent. Once the pellets were washed three times, they were treated at 550 °C with a heating rate of 3° C/min for 6 h. Lastly, the calcined pellets were ground and stored for further characterisation. The sample initially synthesised in DI water (yielding core-shell-like morphology) was named CS-BGNPs whereas the sample synthesised in the 0.3:1 ethanol/water (yielding spherical morphology) was referred to as SP-BGNPs.

Acid-digestion compositional analysis

The compositions of the CS-BGNPs and SP-BGNPs were assessed by acid digestion compositional analysis using a lithium metaborate fusion dissolution method. Briefly, 50 mg of CS-BGNPs or SP-BGNPs were mixed with 250 mg of 80% $LiBiO_2$/20% $Li_2B_4O_7$ in a platinum crucible using a glass rod. The powder mixture was treated for 20 min at 950 °C and subsequently dissolved in 2 M nitric acid. The elemental composition of the solution was then measured using inductively coupled plasma optical emission spectroscopy (ICP-OES; 236 Thermo Scientific iCAP 6000 series).

Characterisation techniques

Bright-field images of both CS-BGNPs and SP-BGNPs were obtained using a JEOL JEM-2100 Plus electron microscope at

200 kV. TEM samples were collected on 400 mesh copper grids coated with a plain carbon film. For each sample, several regions of the TEM grid were imaged, and 50 individual nanoparticles from the same synthetic batch were analyzed using Fiji (Schindelin et al., 2012). The images were first converted to binary format, and the "Analyze Particles" function was applied to measure the area of each particle in square pixels. These values were then converted to particle radius and subsequently to diameters in nanometers.

The size distribution of the nanoparticles and zeta potential (ζ) were determined by dynamic light scattering (DLS) using a Zeta Sizer Nano ZS (Malvern). Each sample was dispersed in ethanol for DLS and in water for zeta potential followed by 30 min of ultrasonication.

The structural characterisation of the nanoparticles was performed using small-angle X-ray scattering (SAXS) and wide-angle X-ray scattering (WAXS) measurements, both conducted on a PANalytical Empyrean diffractometer equipped with a ScatterX 78® attachment and operating under Cu Kα_1 radiation ($\lambda = 1.540598$ Å).

The SAXS configuration employed a 1/32° slit and a focusing mirror optimized for Cu radiation. The SAXS profiles were not background-subtracted.

Scattering patterns were collected using a PIXcel3D Medipix detector in scanning 1D mode. Data acquisition was carried out over a 2θ range of 5°–80°, with a step size of 0.0131° and a counting time of 349 s per step. The resulting patterns encompassed both low-angle (SAXS) and high-angle (WAXS) regions, enabling the assessment of particle morphology and crystallinity, respectively. While SAXS probed nanostructural features such as size, shape, and internal density arising from electron density fluctuations at interfaces (regardless of crystallinity), WAXS captured Bragg diffraction from periodic atomic arrangements in crystalline domains. The WAXS data were analysed by Rietveld refinement using the MAUD software, following appropriate corrections for instrument geometry and scattering intensity to ensure accurate phase identification and quantification.

The Brunauer–Emmett–Teller (BET) method was employed to determine the specific surface area, pore volume, and pore size distribution of the mesoporous nanoparticles. Nitrogen adsorption–desorption isotherms were measured at 77 K using a Quantachrome Autosorb-iQ/MPXR analyzer, with 40 adsorption and 40 desorption points collected over a relative pressure range (P/P_0) of 0.009–0.99. Surface area analysis was performed using the BET multipoint method, while pore characteristics were evaluated using density functional theory (DFT) modeling. The samples were pre-treated by degassing under flowing argon at 200 °C for 24 h (ramp rate: 10 °C/min) to ensure complete removal of moisture and volatiles. The analysis data was performed using P/P_0 values from 0.05 to 0.35.

All ^{29}Si NMR measurements were performed at 7.05 T using a Varian/Chemagnetics InfinityPlus spectrometer operating at a ^{1}H and ^{29}Si Larmor frequency (ν_o) of 300 MHz and 59.6 MHz, respectively. These experiments were performed using a Bruker 7 mm HX probe which enabled a MAS frequency of 5 kHz to be implemented throughout. The ^{29}Si pulse length calibration was performed using solid kaolinite ($Al_2O_3{\cdot}2SiO_2{\cdot}2H_2O$) from which a π/2 pulse time of 4.25 μs was measured. All single pulse measurements were undertaken using a π/4 nutation angle together with a recycle delay of 240 s. For the analogous ^{29}Si CPMAS measurements, an initial ^{1}H π/2 pulse length of 4 μs, a ^{1}H-^{29}Si contact time of 4 ms, and a recycle delay of 10 s were implemented. For all ^{29}Si NMR measurements strong heteronuclear ^{1}H decoupling was applied during the acquisition of all FIDs. The reported ^{29}Si chemical shifts were externally referenced against the IUPAC recommended primary reference of Me_4Si (1% in $CDCl_3$, $\delta_{iso} = 0.0$ ppm) via the secondary solid kaolinite reference ($\delta_{iso} = -92$ ppm)[29]. Quantitative estimates of the Q^n speciation comprising the glass network in the BGNPs was determined using the quantitative ^{29}Si MAS NMR data, with both the degree of condensation (D_c) and network connectivity (NC) being calculated from the measured data.

The corresponding ^{1}H MAS NMR measurements were performed at 14.1 T using a Bruker Avance III-600 spectrometer operating at a Larmor frequency (ν_0) of 600 MHz. These experiments were performed using a Bruker 1.3 mm HXY probe which enabled a MAS frequency of 60 kHz to be implemented. Pulse calibration was performed on solid Alanine from which a π/2 pulse time of 3 μs was measured. All measurements were undertaken with a π/2 nutation angle together with a recycle delay of 3 s. All ^{1}H chemical shifts were externally referenced against the IUPAC recommended secondary solid alanine reference ($\delta_{iso} = 1.1$ ppm) (Harris et al., 2002).

The chemical composition of CS-BGNPs and SP-BGNPs were investigated using a Thermo Fisher Scientific K-Alpha + X-ray Photoelectron Spectroscopy (XPS) operating at 2×10^{-9} mbar base pressure at ambient temperature. The system incorporates a 180° double focusing hemispherical analyser with a 128-channel detector. The Al Kα X-ray source generates a 6 mA emission current with a spot size of 400 μm^2. Pass energies of 200 and 20 were used for the survey and core-level spectra, respectively. The quantitative analyses were performed using Avantage software, V5.9, Thermo Scientific. Shirley background was applied and subtracted from the data. The peaks were fitted using a convolution of Gaussian and Lorentzian peak shapes. C 1*s*, Si 2*p*, Sr 3*d*, Ca 2*p* and O 1*s* were analysed. The binding energies were corrected to the C 1*s* peak position at 284.8 eV originating from surface hydrocarbons.

In vitro cytotoxicity assay

Murine pre-osteoblastic MC3T3-E1 cells were culture expanded in basal α-MEM supplemented with 10% fetal bovine serum (FBS) (v/v), 100 U mL^{-1} Penicillin and 100 μg mL^{-1} Streptomycin in a humidified incubator at 37 °C and 5% CO_2. MC3T3-E1 cells were seeded at a concentration 5×10^4 cells mL^{-1} in a flat-bottomed 96-well plate and incubated for 24 h. The cells were then exposed to different nanoparticles concentrations (0, 0.001, 0.01, 0.1, 1, 10, 100 and 1000 μg mL^{-1}) for 24, 48 and 72 h. Cell viability was measured with the MTT assay, in which the yellow tetrazolium salt is reduced by cells metabolically active to blue formazan crystals; after solubilisation in 100 μL dimethyl sulfoxide the absorbance was recorded at 570 nm using a SpectraMax M2e microplate reader (Molecular Devices).

Effect of CS-BGNPs and SP-BGNPs on osteoblast differentiation

ALP activity served as the indicator of osteogenic differentiation. MC3T3-E1 cells were seeded in 24-well plates. Wells cultured in α-MEM containing 100 μM L-ascorbic acid, 10 mM β-glycerophosphate

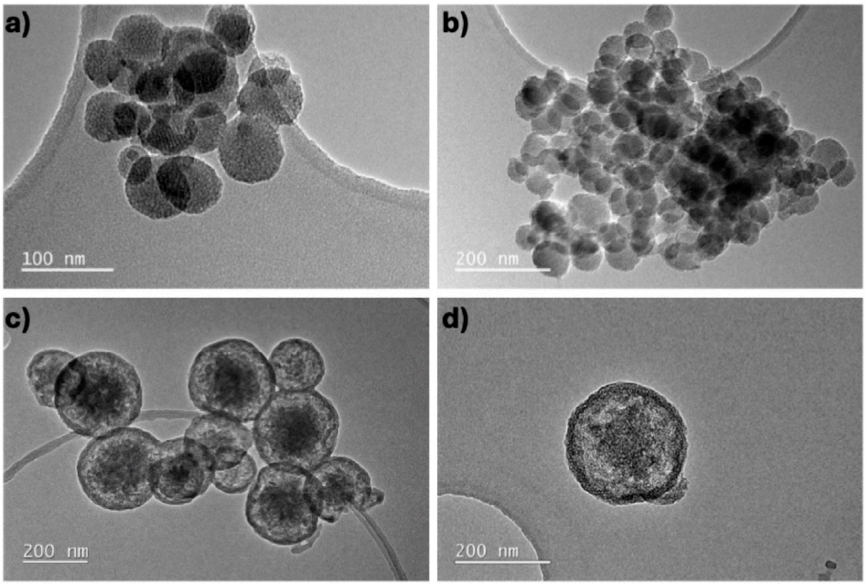

FIGURE 1
Bright field TEM images of **(a,b)** SP-BGNPs (4.99 CaO mol%, 86.73 SiO_2 mol%, 8.28 SrO mol%) and **(c,d)** CS-BGNPs (4.94 CaO mol%, 85.38 SiO_2 mol%, 9.68 SrO mol%).

and 10 nM dexamethasone acted as the osteogenic positive control. Test wells were treated using two exposure methods. In the first method, cells were exposed to 0.1 μg mL^{-1} of either CS-BGNPs or SP-BGNPs in basal medium for 24 h. The suspension was then replaced with fresh basal α-MEM, and the cells were cultured for 7, 14, or 21 days, with medium changes every 3 days. In the second method, 0.1 μg mL^{-1} of CS-BGNPs or SP-BGNPs were pre-incubated in basal medium for 24 h. The resulting particle-free supernatant, containing the released ions, was collected and added to the cells for incubation over the same time points. ALP activity was measured at each time point using a commercial kit (Merck Life Science, UK) in accordance with the manufacturer's protocol.

Assessment of BGNPs radical-scavenging capability

The antioxidant activity of CS-BGNPs and SP-BGNPs was assessed in MC3T3-E1 cells with the DCFDA cellular reactive-oxygen-species assay. Cells were seeded at 1.5 × 10^5 per well, loaded with 20 μM DCFDA, and exposed to 50 μM tert-butyl hydroperoxide (TBHP) to generate oxidative stress. Cultures were then supplemented with osteogenic factors and treated with either CS-BGNPs or SP-BGNPs at 0.1 μg mL^{-1}. After 24 h, fluorescence was measured on a plate reader (λ_{ex} 495 nm, λ_{em} 529 nm). TBHP converts the non-fluorescent DCFDA to fluorescent DCF; thus, lower fluorescence denotes greater radical-scavenging by the nanoparticles.

Statistical analysis

All *in vitro* results are expressed as mean ± standard deviation, based on three independent replicates for each condition (n = 3). Differences among multiple groups were assessed with one-way ANOVA followed by Tukey's *post hoc* test, while pairwise comparisons were evaluated with the Student's t-test.

Results and discussion

CS-BGNPs and SP-BGNPs synthesis and characterisation

A one-pot modified Stöber method was employed to synthesise nanoparticles incorporating Ca and Sr therapeutic ions. Variations in solvent composition during synthesis influenced both the morphology and size of the resulting nanoparticles. TEM analysis of SP-BGNPs synthesised using an ethanol/water solvent mixture (Figures 1a,b) revealed spherical nanoparticles with an average diameter of 74 ± 5 nm, that exhibited a tendency to form agglomerates. In contrast, CS-BGNPs synthesized in water alone formed significantly larger spherical particles, with an average diameter of 224 ± 42 nm, and displayed a core–shell-like structure. (Figures 1c,d). Solvent variation also affected the intra-particle pore morphology, with SP-BGNPs exhibiting parallel-aligned pores, while CS-BGNPs displayed a worm-like pore structure, consistent with observations reported by Schumacher et al. (2021). The hydrodynamic diameter and zeta potential of CS-BGNPs were measured at 227.6 ± 17.5 nm and −12.7 ± 3.9 mV, respectively, while SP-BGNPs at 91.8 ± 5.8 nm and −18.5 ± 3.3 mV. All measurements were conducted with samples dispersed in water at pH 6.8 (Table 1). The observed difference between TEM and DLS size measurements is attributed to particle agglomeration in aqueous suspension, which affects the hydrodynamic diameter captured by DLS. This effect was particularly pronounced in the SP-BGNPs, despite their smaller

TABLE 1 Zeta potential, hydrodynamic diameter (Polydispersity Index (PDI) 0.2 SP-BGNPs, 0.4 to the CS-BGNPs), and elemental composition of CS-BGNPs and SP-BGNPs characterised by DLS and ICP-OES.

Sample	DLS		ICP-OES			
	ζ-Potential (mV)	Size(nm)	Ca (mol%)	Si (mol%)	Sr (mol%)	Total (mol%)
CS-BGNPs	−12.7 ± 3.9	227.6 ± 17.5	4.94	85.38	9.68	100.00
SP-BGNPs	−18.5 ± 3.3	91.8 ± 5.8	4.99	86.73	8.28	100.00

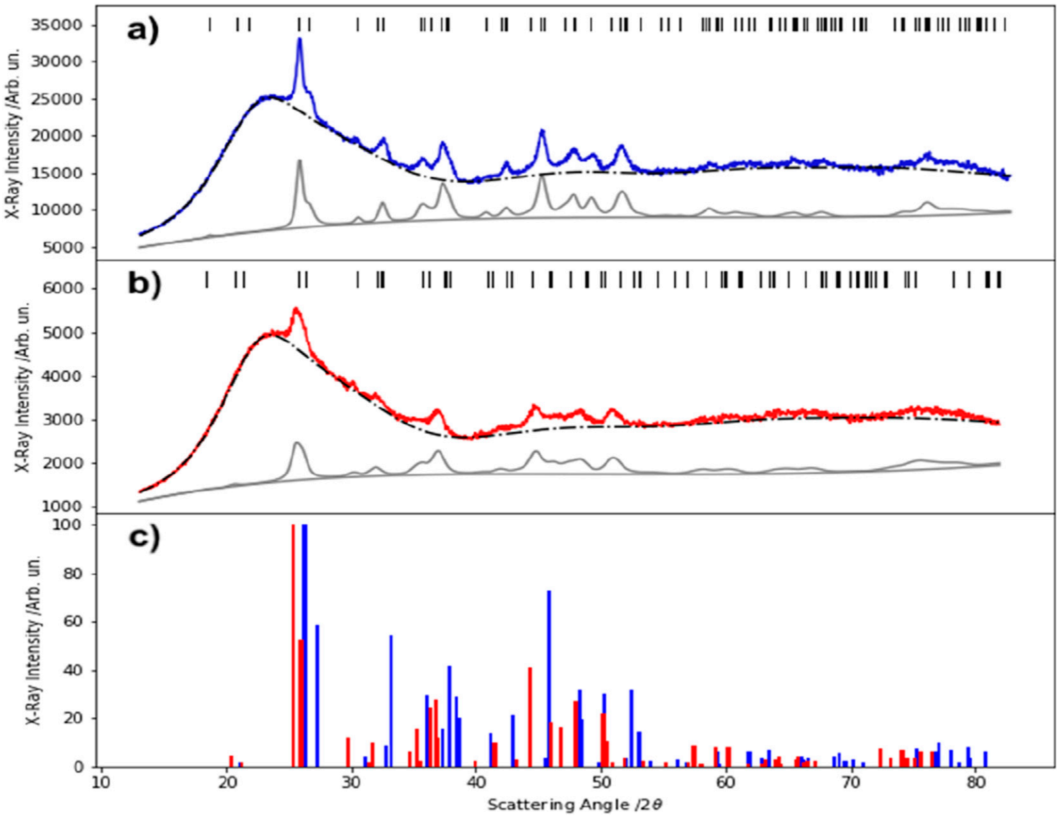

FIGURE 2
Rietveld refinement of WAXS patterns for **(a)** SP-BGNPs (blue) and **(b)** CS-BGNPs (red). The broad feature corresponds to the amorphous silica phase (black dotted line), while the calculated patterns from MAUD are shown in grey, and the refined Bragg reflections are marked by black bars. **(c)** Reference diffraction patterns of Aragonite (blue) and Strontianite (red) are included for comparison. WAXS and XRD both provide crystallographic information, the WAXS data here were collected using wide-angle scattering geometry and refined accordingly[34].

primary particle size, likely due to variations in surface charge that influence colloidal stability. Furthermore, the Polydispersity Index (PDI) of 0.4 for CS-BGNPs indicates a broader and more heterogeneous particle population, while the lower PDI of 0.2 for SP-BGNPs reflects a narrower size distribution and more uniform morphology. The DLS intensity-based size distribution profiles (Supplementary Figure S1) further illustrate the broader distribution and presence of aggregates in the CS-BGNPs, suggesting that the higher PDI arises primarily from particle clustering rather than intrinsic size variation.

The measured zeta potentials are consistent with previously reported values for bioactive glass nanoparticles of comparable composition and tested under similar conditions (Antoniac, 2016; Naruphontjirakul et al., 2016). Zeta potential values are generally categorized into three colloidal stability regimes: nanoparticles with zeta potentials between +10 mV and −10 mV are considered electrically neutral and prone to aggregation; those within the ±30 mV range exhibit moderate colloidal stability but may still aggregate over time due to van der Waals forces; whereas particles with zeta potentials beyond ±30 mV demonstrate high colloidal stability and strong repulsive interactions (Clogston and Patri, 2010; Rodriguez-Loya et al., 2023). As the zeta potentials of both CS-BGNPs and SP-BGNPs fall within the ±30 mV range, a moderate degree of aggregation is expected for both. Interestingly, the greater tendency of SP-BGNPs to form aggregates—despite their higher absolute zeta potential—may be due to ethanol-induced changes in surface chemistry that reduce steric or electrostatic stabilization. Conversely, the relatively lower agglomeration observed in CS-BGNPs may result from their larger size and the stabilizing effects of using water as the sole solvent during synthesis.

Despite the distinct morphological differences observed between CS-BGNPs and SP-BGNPs, their elemental compositions (Table 1) remained largely unaffected by the choice of solvent. The molar percentages (mol%) of key constituents, including Ca, Si, and Sr, were comparable between both nanoparticle groups. This indicates that solvent variation during synthesis had a negligible impact on the overall chemical composition of the BGNPs.

The structural analysis of both SP-BGNPs and CS-BGNPs compositions was performed using small-angle X-ray scattering (SAXS) and wide-angle X-ray scattering (WAXS). The WAXS measurement reported in Figures 2a,b were analysed by Rietveld refinement (black bars), enabling the identification of amorphous and crystalline phases. The broad shoulder ranging from ~15° 2θ to ~30° 2θ is associated with the presence of amorphous silica domains within the nanoparticles, indicating that the samples are predominantly amorphous. In addition, sharp reflections were observed, indicative of crystalline domains formed through incorporation of Ca^{2+} and Sr^{2+} cations. These Bragg peaks were matched to reference patterns (Figure 2c) reported by De Villiers (1971) and correspond to two crystalline phases: Aragonite ($CaCO_3$; JCPDS 76-0606) and Strontianite ($SrCO_3$; JCPDS 84-1778), both belonging to the PMCM space group (Downs and Hall-Wallace, 2003). Since Ca^{2+} and Sr^{2+} act as network modifiers, not formers, they do not alter the silica matrix structure but reduce Si–O–Si connectivity by balancing non-bridging oxygen atoms, which may influence dissolution and bioactivity, despite the dominant amorphous halo in WAXS. Commonly, small amounts of Aragonite can be formed through atmospheric carbonation during sol–gel synthesis resulting in crystalline phases (Hurt et al., 2014; Li et al., 2015). The relative intensities of the peaks were similar to the reference patterns (Figure 2c), though a shift in angular positions was observed. This can be attributed to lattice strain and stoichiometric variation imposed on the amorphous mesoporous silica network by the incorporation of Ca^{2+} and Sr^{2+} ions (Boyd et al., 2015). Microstrain was evaluated by Rietveld refinement under the assumption of isotropic strain, which is appropriate for the resolution of our data. The calculated strain reflects peak broadening across various crystallographic planes (hkl) and should not be confused with peak position or “crystallinity”. Although the first diffraction peak (~26.3° 2θ) appears more shifted in SP-BGNPs than in CS-BGNPs, this shift results from changes in average lattice parameters, not strain magnitude. The apparent contradiction—where CS-BGNPs contain more Sr^{2+} but show less peak shift—may be due to a larger fraction of Sr^{2+} being incorporated into crystalline domains in SP-BGNPs, resulting in a greater structural impact despite their lower total Sr content. The two identified crystalline phases, Aragonite and Strontianite, are biocompatible and have been shown to stimulate osteoblast differentiation and activity while inhibiting osteoclast-mediated bone resorption (Shafiu Kamba and Zakaria, 2014; Maçon et al., 2017; Zeng et al., 2020). Sr^{2+} substitutes for Ca^{2+} within the Aragonite structure which dilates the lattice by 2% and permits higher uptake of water, leading to higher dissolution rates in aqueous media (Antoniac, 2016; Tovani et al., 2018). Additionally, Sr^{2+} increases the metabolic activity of osteoblasts and suppresses the osteoclast resorption of bone (Gentleman et al., 2010). The Ca^{2+} ion in the Aragonite lattice within the silica network improves osteointegration and osteoconduction, which results in the higher production of Ca^{2+}-based films that stimulate the formation of native bone by osteoblasts (Shafiu Kamba and Zakaria, 2014). Furthermore, the BGNPs doped with Ca^{2+} ions create bonds with native tissue that lead to the formation of biological apatite and stimulation of osteoprogenitors to differentiate into osteoblasts (Shafiu Kamba and Zakaria, 2014). In summary, despite the presence of Aragonite and Strontianite phases at levels below 15% within the silica framework (Table 1), the overall chemical composition of the BGNPs remains largely unchanged, with only minor variations observed in crystallinity.

SAXS, plotted on a bi-logarithmic scale (Figure 3), was used to assess the nano-structural properties such as size, shape, and internal density of SP-BGNPs and CS-BGNPs (Rice et al., 1956). The SAXS profiles were not background-subtracted, and differences in scattering intensity onset likely result from sample concentration or electron density contrast. It is important to note that SAXS measures the scattering of X-rays due to electron density fluctuations at interfaces between different phases (e.g., particle and void), regardless of the internal atomic ordering (i.e., crystalline or amorphous). SAXS probes these differences in electron density by analysing the scattering-intensity profile, I(Q) versus Q, across distinct scattering regimes. As a result, SAXS data reflect features such as particle morphology, internal structure, and size distribution, but not crystallographic ordering. It should be kept in mind that SAXS (commonly referred to as the (000) reflection, as the origin of the reciprocal space) arises from squared electron density fluctuations at interfaces or within particles. In contrast, Bragg peaks associated with atomic periodicity are observed at higher scattering angles in WAXS measurements and originate from the periodic arrangement of atoms in crystalline domains.

The first region of interest is the Guinier regime that occurs at low scattering angles of $Q < 0.4\ nm^{-1}$. The second region of interest is the Porod regime which encompasses scattering within the range from $0.7 < Q < 2\ nm^{-1}$. Normally, an increase in the intensity at low Q relates to an increase in the size and/or the number of nanoparticles. The SAXS results show that SP-BGNPs (pink line) and CS-BGNPs (blue line) exhibit scattering profiles that approximate a −2 slope, suggestive of surface fractal characteristic (Corenblit et al., 2011). However, despite this similarity in slope, distinct structural differences between the two nanoparticle systems are evident: TEM and compositional analysis indicate a core–shell-like architecture in CS-BGNPs, whereas SP-BGNPs display a more homogeneous internal structure. The −4 slope in Figure 3 (green line) is based on Porods Law (Porod, 1951), which is followed only when scattering arises from an ideal two-phase system with perfectly sharp interfaces; porous or surface-fractal particles deviate from this, as seen here. For example, porous nanoparticles would have solid matter with constant electron density whereas their pores would have zero density. The pores in the nanometre range would result in the scattering (Li et al., 2001).

The results presented in Figure 3 indicate that nanoparticles synthesized in water (CS-BGNPs) were larger than those produced using the water/ethanol co-solvent (SP-BGNPs), consistent with the DLS data in Table 1 and the TEM observations. Additionally, CS-

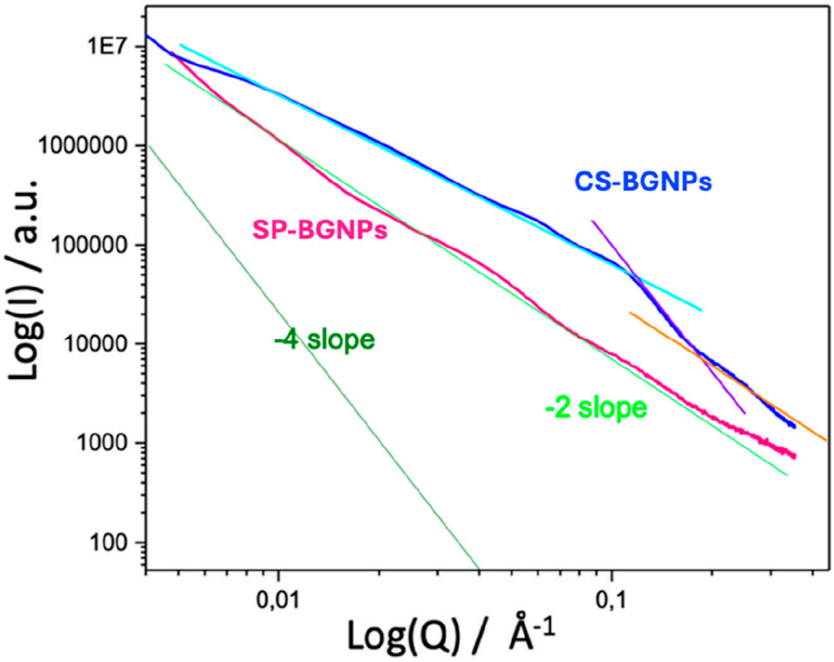

FIGURE 3
SAXS pattern of SP-BGNPs (pink line) and CS-BGNPs (blue line). The intensity is a function of the scattering vector Q. The −4 slope (green line) is based on Porods Law and is used for comparison.

BGNPs exhibited a higher internal density compared to SP-BGNPs. Furthermore, the observed low-q upturn suggests some degree of particle aggregation. Although no model-based fitting was performed, the presence of a characteristic knee at q ≈ 0.11 $Å^{-1}$ (corresponding to ~5.5 nm) suggests an internal structural feature. Given that the core–shell like configuration of SP-BGNPs is supported by SAXS and TEM data.

Surface area and porosity of both CS-BGNPs and SP-BGNPs were characterised by gas sorption analysis. The isotherms presented in Figure 4, evaluated in accordance with the IUPAC classification (Thommes et al., 2015), indicate that SP-BGNPs exhibit a Type III isotherm, characteristic of weak adsorbate–adsorbent interactions and typically associated with nonporous or macroporous materials. In contrast, the CS-BGNPs isotherm corresponds to a Type IV(a) profile with an H4-type hysteresis loop, suggesting the presence of slit-like mesopores and potential microporosity (Rice et al., 1956; Orcel et al., 1988).

The substitution of 0.3 mol of water with ethanol during the synthesis significantly influenced the textural properties of the nanoparticles. Specifically, the surface area of the SP-BGNPs was measured at 10.46 m^2/g, substantially lower than the 202.82 m^2/g recorded for the CS-BGNPs synthesized exclusively in water (Table 2). This marked increase in surface area for CS-BGNPs correlates with corresponding enhancements in pore volume and average pore size. The pore volume increased from 0.03 $cm^3\ g^{-1}$ in BGNPs to 0.38 $cm^3 g^{-1}$ in CS-BGNPs, while the average pore diameter expanded from 1.69 nm to 3.79 nm, respectively. These results indicate that the presence of ethanol as a co-solvent during synthesis leads to denser nanoparticles with reduced porosity, whereas synthesis in pure water favours the formation of nanoparticles with larger surface area and more developed porous structures. The observed differences in porosity and surface area are expected to affect both the bioactivity and degradation behaviour of the nanoparticles. Specifically, the higher surface area and mesoporous structure of CS-BGNPs may promote greater ion release and enhanced osteogenic differentiation (Hoppe et al., 2011; Polo-Montalvo et al., 2021) whereas the denser, less porous SP-BGNPs—with their smaller and more uniform morphology—are likely to exhibit better biocompatibility due to slower degradation (Polo-Montalvo et al., 2021).

Chen et al. demonstrated that the ethanol-to-water ratio in a one-pot modified Stöber synthesis markedly influences the kinetics of hydrolysis and condensation reactions, thereby affecting the formation of mesoporous silica shells (Chen et al., 2018). Their results highlight that variations in solvent composition can alter nanoparticle size, morphology, and surface area. Consistent with these findings, our study observed that while solvent choice impacted nanoparticle morphology (Figure 1), the incorporation of Ca^{2+} and Sr^{2+} ions within the silica network remained unaffected (Figures 5, 6).

Similarly, Khodaee et al., reported that ethanol as a co-solvent enhances control over nanoparticle size and shape (Khodaee et al., 2018). An increased ethanol: water ratio at constant temperature yields larger, more uniform spherical nanoparticles but leads to decreased surface area and pore volume. Our results corroborate these observations: SP-BGNPs synthesized in an ethanol/water mixture exhibited smaller, more monodisperse particles compared to the larger, agglomerated CS-BGNPs produced in pure water. Furthermore, the reduction in surface area, pore volume, and pore size with ethanol use aligns with prior reports. The presence of crystalline phases within the

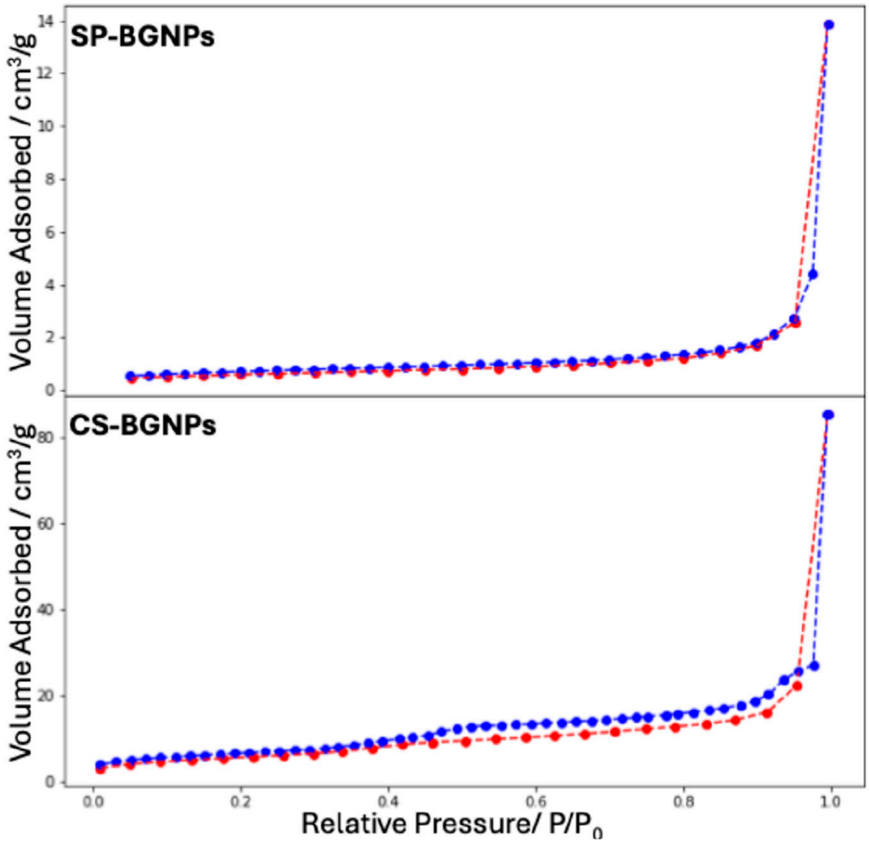

FIGURE 4
Nitrogen adsorption (red dotted-line) and desorption (blue dotted-line) isotherms obtained for both SP-BGNPs (Top) and CS-BGNPs (Bottom).

TABLE 2 Surface area, pore volume and pore size calculated by BET-Multipoint and DFT method of both BGNPs samples.

Sample	BET-multipoint analysis	DFT method	
	Surface area (m^2/g)	Pore volume (cm^3/g)	Pore size (nm)
CS-BGNPs	202.82	0.38	3.79
SP-BGNPs	10.46	0.03	1.69

nanoparticles may also contribute to variations in their adsorption properties, as these phases can disrupt the uniformity of the mesoporous network and influence surface chemistry. Moreover, the use of water versus a water–ethanol mixture during synthesis affects the nucleation and growth kinetics of these crystalline domains. Ethanol, acting as a co-solvent, slows down hydrolysis and condensation reactions, leading to more uniform and denser particles with finely dispersed or limited crystallinity. In contrast, synthesis in pure water promotes faster reaction kinetics, favoring the formation of larger or more clustered crystalline regions. These differences in crystallinity distribution directly impact the spatial organization of amorphous and crystalline domains, ultimately influencing the surface area and porosity of the nanoparticles (Khamsehashari et al., 2018; Thanasrisuebwong et al., 2022; Zadsirjan et al., 2024).

Silica structure evolution and H species chemical composition in CS-BGNPs and SP-BGNPs

^{29}Si MAS NMR data (Table 3) was acquired to quantify the degree of condensation (D_c), network connectivity (NC) and bridging oxygen fraction (BO) of the silica network structure of CS-BGNPs and SP-BGNPs. D_c, NC, and BO were calculated using the equations below (Nesbitt et al., 2011; Ruiz-Clavijo et al., 2019):

$$\text{Degree of condensation: } D_c = \frac{Q^1\% + 2Q^2\% + 3Q^3\% + 4Q^4\%}{4}$$

$$\text{Network connectivity: } NC = \frac{Q^1\% + 2Q^2\% + 3Q^3\% + 4Q^4\%}{100}$$

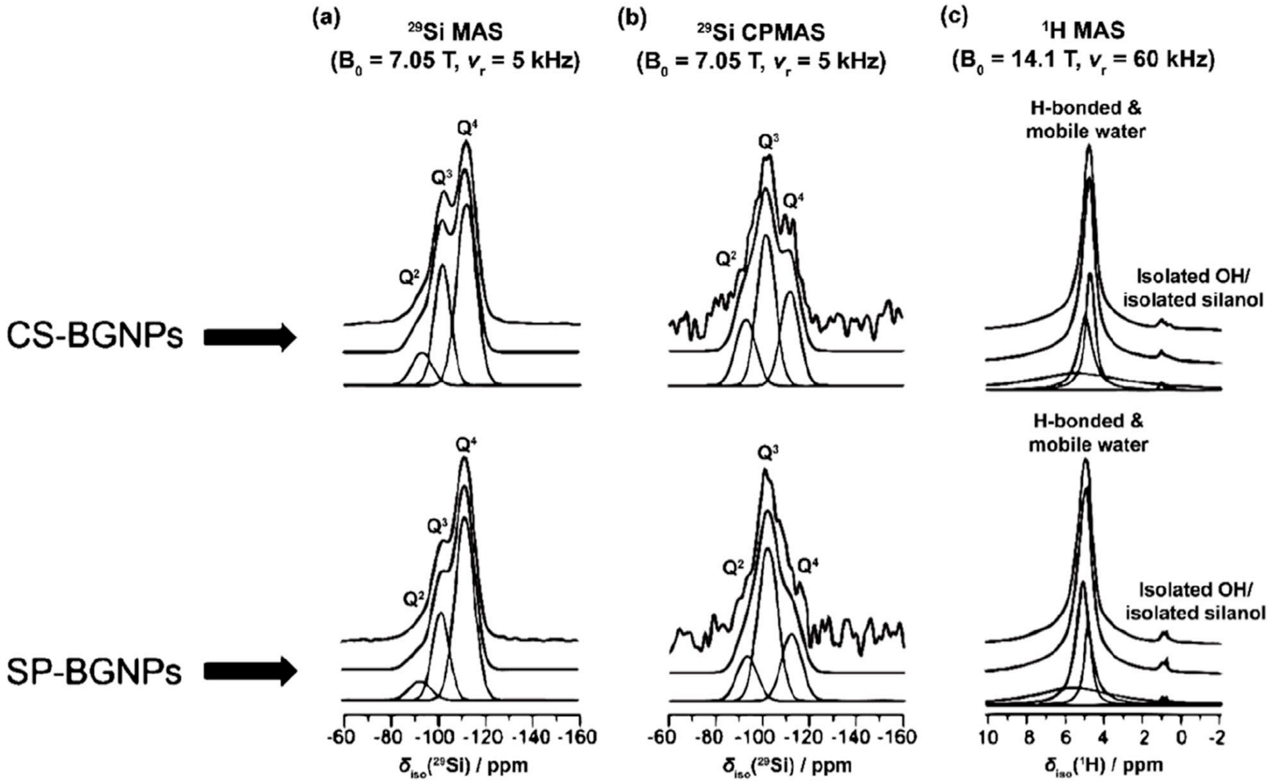

FIGURE 5
The **(a)** ^{29}Si MAS NMR data, (B_0 = 7.05 T, ν_r = 5 kHz), **(b)** ^{29}Si CPMAS NMR data (B_0 = 7.05 T, ν_r = 5 kHz), and **(c)** ^{1}H MAS NMR data (B_0 = 14.1 T, ν_r = 60 kHz) measured for the CS-BGNPs and SP-BGNPs.

$$\text{Bridging Oxygen fraction: BO} = \frac{(0.5{*}Q^1\% + 1.0{*}Q^2\% + 1.5{*}Q^3\% + 2.0{*}Q^4\%)}{(4.0{*}Q^0 + 3.5{*}Q^1\% + 3.0{*}Q^2\% + 2.5{*}Q^3\% + 2.0{*}Q^4\%)}$$

Non-bridging oxygen species (NBO) were calculated as NBO = (1 – BO). The Q species describes the connectivity of the silica network within the BGNPs, where Q^n denotes a silicon with n bridging oxygens. BO bonds form when an oxygen atom is bonded with two silica atoms in the silicate network (Si-O-Si). The incorporation of metal ions as network modifiers can disrupt the silica network resulting in the formation of NBOs (Dalby et al., 2007; Barrioni et al., 2022). Therefore, the incorporation of various network modifiers will alter the proportions of BO and NBO, impacting the proportion of Q^n species in the silica network (Shafiu Kamba and Zakaria, 2014). Figure 5a presents the ^{29}Si MAS NMR spectra and the calculated percentage of Q^n species is shown in Table 3. The proportions of each Q^n species were obtained by the deconvolution of the ^{29}Si MAS NMR spectra. Two distinct regions can be observed from the ^{29}Si MAS NMR data at δ_{iso} ~ −101 ppm and δ_{iso} ~ −111 ppm, indicating Q^3 and Q^4 species respectively for both CS-BGNPs and SP-BGNPs. A less prominent Q^2 species peak can be observed at δ_{iso} ~ −93 ppm for both samples, with no Q^1 found in either sample. These results indicate a highly condensed silica network compared to previously reported work for pure silica nanoparticles[60]. Hence, the incorporation of these ions promotes greater network condensation and connectivity, accounting for the increased density observed in our materials.

The SP-BGNPs show an even higher degree of Q^4 species relative to CS-BGNPs, with a lower Q^3/Q^4 ratio suggesting that SP-BGNPs have a denser and more highly connected network, leading to D_c = 89.4 for SP-BGNPs compared to D_c = 86.6 for CS-BGNPs. The D_c values suggest that the influence of the solvents used during synthesis can impact the connectivity of the silica network. CS-BGNPs synthesised with water as a solvent exhibited a less dense network relative to SP-BGNPs that were synthesised using a mixture of ethanol/water. Consistently, the calculated network connectivity rises from 3.5 for CS-BGNPs to 3.6 for SP-BGNPs. Although the ideal NC for fully condensed SiO_2 is 4, sol-gel-derived silica retains many silanol (Si–OH) groups that cap non-bridging oxygens and therefore lower the average connectivity.

The SP-BGNPs show a larger fraction of bridging oxygens (BO) and a smaller fraction of non-bridging oxygens (NBO) than the CS-BGNPs. In silicate glasses, a higher NBO content usually signals that more Ca^{2+} and Sr^{2+} ions remain in the glassy network as modifiers that break Si–O–Si bridges. The greater NBO fraction in CS-BGNPs therefore points to a larger share of modifiers inside the network, whereas in the SP-BGNPs part of the Ca and Sr has crystallised as Aragonite and Strontianite. This partial removal of modifiers leaves the SP-BGNP silica framework more fully condensed, consistent with its higher Dc value (89.4 versus 86.6) and the slightly higher network connectivity NC (3.6 versus 3.5). If all CaO and SrO were

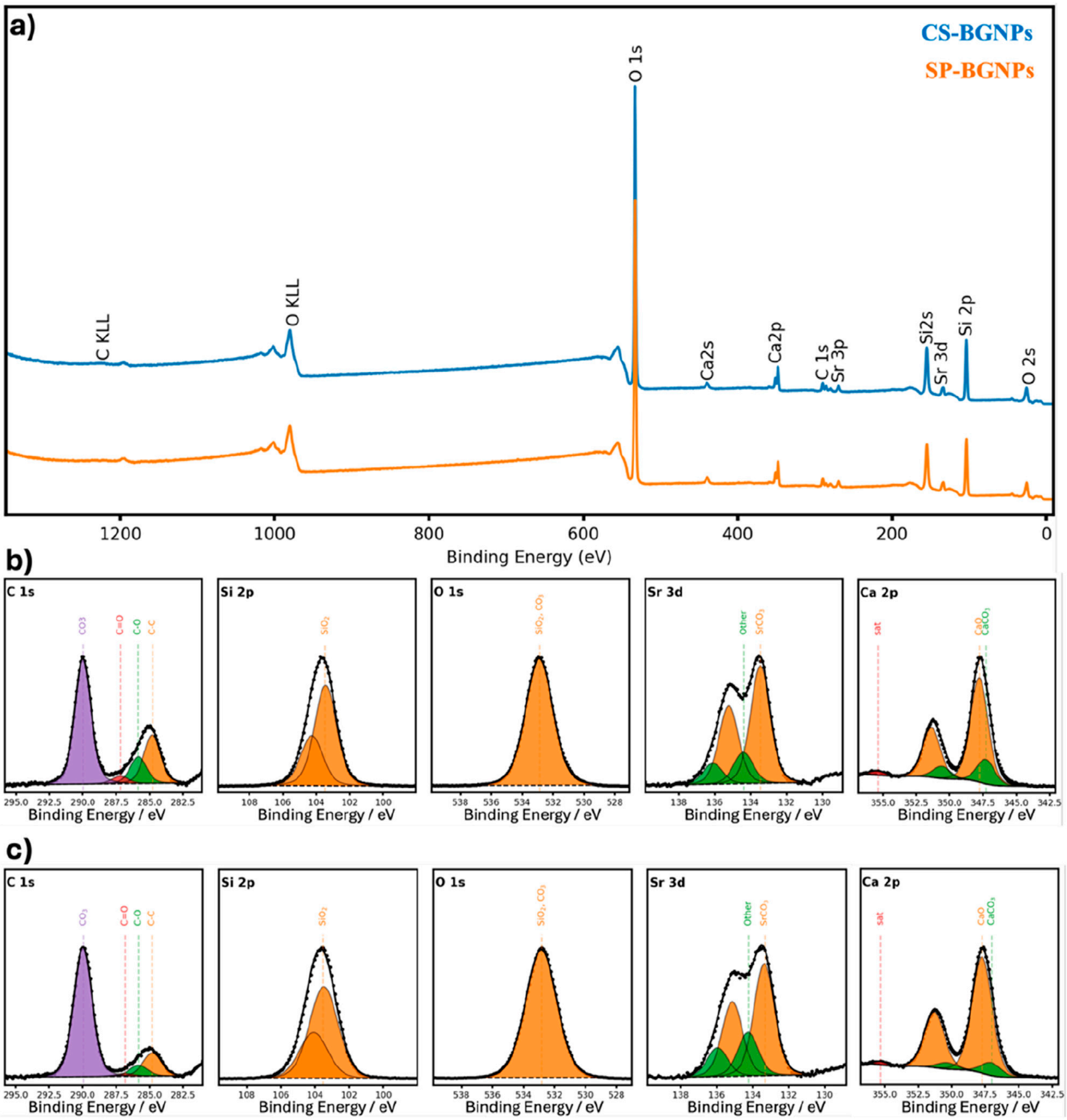

FIGURE 6
(a) Survey scan spectra X-ray of CS-BGNPs (blue line) and SP-BGNPs (orange line). High-resolution X-ray Photoelectron Spectroscopy (XPS) C 1s, Si 2p, O 1s, Sr 3d and Ca 2p spectra of **(b)** CS-BGNPs and **(c)** SP-BGNPs.

retained in the glass, the theoretical NC calculated from the compositions in Table 1 would be about 3.7 for both samples. The experimental values fall below this limit because the sol-gel route leaves silanol (Si–OH) groups that cap non-bridging oxygens, and because some Ca^{2+} and Sr^{2+} are sequestered in carbonate crystals instead of acting as modifiers (Chen et al., 2018). The ^{29}Si CPMAS and ^{1}H MAS NMR data in Figures 5b,c, give additional insight into hydrogen speciation. Most H species in both samples are present as both H-bonded and mobile water with less than 2% as isolated OH^-/silanol species. The H species are located closer to Q^3 species than Q^2 and Q^4 which causes the enhancement in the CPMAS spectra of the Q^3 resonance at $\delta_{iso} \sim -101$ ppm. The signal enhancement in the CPMAS experiment is poor, which indicates that there is inefficient transfer of polarisation caused by modulation in the heteronuclear dipolar interaction via water mobility. The reduced enhancement occurs in both CS-BGNPs and SP-BGNPs, showing that the addition of ethanol as a solvent does not affect the mobility of water within the samples. The ^{1}H MAS NMR spectra are similar for CS-BGNPs and SP-BGNPs showing that the solvent mixture does not affect the H speciation despite the difference in the silicate network.

TABLE 3 Percentage of Q^n Si species, degree of condensation (D_c), network connectivity (NC) and bridging (BO) and non-bridging oxygen (NBO) fractions determined from the single pulse^{29}Si MAS NMR (υ_r = 5 kHz) data, for SP-BGNPs and CS-BGNPs. The percentage and assignments of the H species determined from the ^{1}H MAS NMR data, B_0 = 14.1 T, υ_r = 60 kHz and^{29}Si MAS NMR data, B_0 = 7.05 T, υ_r = 5 kHz.

Samples	Q^2		Q^3		Q^4		Q^3/Q^4	D_c [%]	NC [%]	BO	NBO
	δ_{iso} [ppm]	I [%]	δ_{iso} [ppm]	I [%]	δ_{iso} [ppm]	I [%]					
CS-BGNPs	−92.8	10.7	−101.4	32.2	−111.6	57.1	0.6	86.6	3.5	0.75	0.25
SP-BGNPs	−93.0	7.6	−101.8	27.2	−111.9	65.2	0.4	89.4	3.6	0.79	0.21
^{1}H MAS NMR data, B_0 = 14.1 T, υ_r = 60 kHz											
	δ_{iso} [ppm]	I [%]	Proton species								
CS-BGNPs	0.64	0.49	Isolated silanol								
	0.85	0.08									
	1.06	0.86									
	4.68	32.3	Hydrogen bonded water								
	4.92	30.55									
	5.35	35.71	Hydrogen bonded silanol								
SP-BGNPs	0.82	0.33	Isolated silanol								
	1	1.11									
	3.61	0.19	Physiosorbed water								
	4.79	18.18	Hydrogen bonded water								
	5.06	48.47									
	5.51	31.72	Hydrogen bonded silanol								

TABLE 4 Quantification of atomic ratios based on the binding energy of the constituents from (a) CS-BGNPs and (b) SP-BGNPs measured by XPS.

XPS Core-Level Peak Ratio (Element: Reference State)	(a) CS-BGNPs atomic ratio (%)	(b) SP-BGNPs atomic ratio (%)
Si $2p_{3/2}$ SiO_2: Sr $3d_{5/2}$	97.8: 2.2	97.7: 2.3
Ca $2p_{3/2}$: Si $2p_{3/2}$ SiO_2	8.6: 9.4	9.5: 90.5
C $1s$ CO_3: Ca $2p_{3/2}$ $CaCO_3$	86.8: 1.,2	92.2: 7.8

X-ray photoelectron spectroscopy (XPS) was used to characterise the surface chemistry of CS-BGNPs and SP-BGNPs. The survey spectra in Figure 6a contains only Si, O, Ca, Sr and a small adventitious-carbon signal, confirming the absence of extraneous elements; the corresponding surface atomic ratios are listed in Table 4. High-resolution spectra (Figure 6b for CS-BGNPs; Figure 6c for SP- BGNPs) reveal Ca $2p_{3/2}$ centred at ≈ 347 eV and Sr $3d_{5/2}$ at ≈ 134 eV, binding energies slightly higher than those of $CaCO_3$ and $SrCO_3$ but typical of Ca–O–Si and Sr–O–Si linkages. The O 1s envelope resolves into a main Si–O–Si component at about 533 eV. The presence of carbonate species at 531.5 eV cannot be resolved in the O1s but can be clearly identified in the C1s spectra at a binding energy of 289 eV. The C–C and C–O peaks at 284.8 eV and 286–287 eV arise from surface hydrocarbons and serve for charge correction[61]. The Si 2p doublet appears at 103.4 eV for both samples, fully consistent with oxidised silicon in a silicate network (Toufiq et al., 2013). Sr3d shows a high amount of SrCO3 at binding energy of 133.5 eV corresponding to the CO_3 peak in the C1s. Together, these features show that Ca^{2+} and Sr^{2+} are bonded to non-bridging oxygens within the glassy matrix—that is, they act as network modifiers, while only minor carbonate species reside on the particle surface.

The resulting atomic ratios for CS-BGNPs and SP-BGNPs are summarised in Table 4. There was no significant difference in the atomic ratios between Sr and Si in both samples, indicating a similar amount of Sr ions were incorporated into the chemical structure. However, there was a slightly higher atomic ratio between Ca and Si in SP-BGNPs (9.5: 90.5) relative to CS-BGNPs (8.6: 91.4). This suggests the synthesis route for SP-BGNPs may result in a higher incorporation of Ca ions, relative to CS-BGNPs. This confirms the ICP-OES (Table 1) and ^{29}Si MAS NMR results (Figure 5). Overall, the XPS results confirm that switching from water to an ethanol/water co-solvent does not produce a substantive change in the way Ca and Sr are incorporated into the silicate framework.

XPS evaluation showed that Sr and Ca are both present as modifiers in the bioactive glass network of CS-BGNPs and SP-

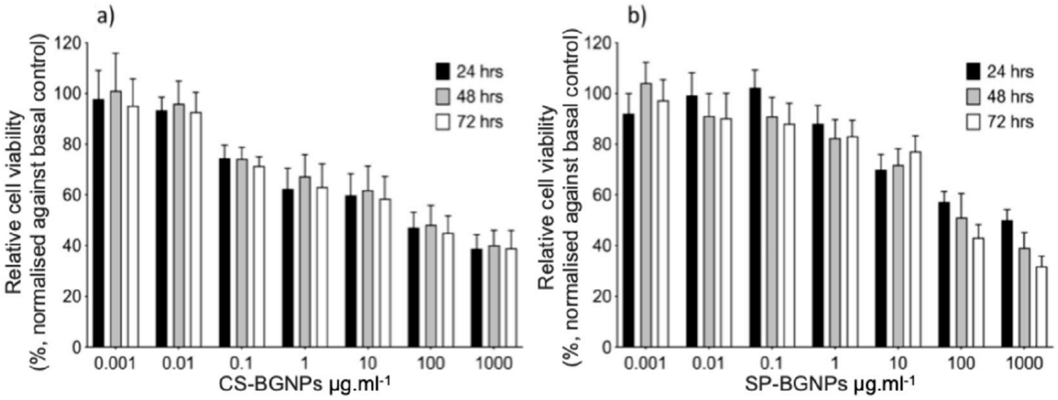

FIGURE 7
Cell viability of MC3T3-E1 cells exposed to **(a)** CS-BGNPs and **(b)** SP-BGNPs for 24 h, 48 h and 72 h measured using the MTT assay, normalised to the control (cells not treated). The data are expressed as mean ± SD of three independent experiments (n = 6). Bars exceeding 100% indicate higher metabolic activity compared to control, possibly due to enhanced cell proliferation or mitochondrial activity. (*) Indicates a statistically significant difference compared to controls ($p < 0.05$).

BGNPs. No significant structural network changes were observed due to the incorporation of Sr and Ca ions between the two samples, as the O *1s* and Si *2p* spectra exhibit similar features and binding energies to those of previously reported bioactive glass nanoparticles (Queiroz et al., 2023). This advantageously preserves osteogenic functionality while allowing morphological tuning. Furthermore, this synthetic process enables adaptation of nanoparticle morphology to specific applications, with core-shell-like designs providing improved encapsulation and controlled release without compromising silica shell bioactivity (Talib et al., 2025).

Cellular toxicity of BGNPs and SP-BGNPs

The biocompatibility of CS-BGNPs and SP-BGNPs was evaluated in MC3T3-E1 osteoblast cells using the MTT metabolic activity assay. As shown in Figures 7a,b, after 72 h of treatment, CS-BGNPs induced significantly reduced cellular metabolic activity at concentrations above 0.1 g mL^{-1} while SP-BGNPs did not cause statistically significant adverse effects at any concentration of up to 10 g mL^{-1}. This difference could be due to the morphological differences between CS-BGNPs and SP-BGNPs with size dependent changes in viability. In general, larger particles such as CS-BGNPs resulted in a greater reduction of cell viability than smaller particles such as SP-BGNPs after 24 h of exposure (Barrioni et al., 2022). Concentrations up to 0.1 g mL^{-1} of both CS-BGNPs and SP-BGNPs did not significantly reduce cell viability (viability remained above 70% of that of the control), therefore subsequent assays measuring ALP and ROS were conducted at a concentration of 0.1 g mL^{-1}.

Assessment of BGNPs osteoblastic activation and radical-scavenging capability

The osteogenic response to CS-BGNPs and SP-BGNPs was evaluated by measuring ALP activity in MC3T3-E1 pre-osteoblasts (Figure 8a). Two exposure methods were evaluated. In the particle condition, cells were cultured with 0.1 μg mL^{-1} of either CS-BGNPs or SP-BGNPs for 24 h. The suspension was then replaced with fresh basal α-MEM, and the cells were cultured for 7, 14, or 21 days. In the dissolution condition, nanoparticles were first incubated in basal medium for the same durations, after which the particle-free supernatant, containing ions released during incubation, was collected and added to the cells for incubation over the same time points. Basal medium and osteogenic medium supplemented with ascorbic acid, dexamethasone and β-glycerophosphate served as negative and positive controls, respectively. After 21 days the dissolution media from both nanoparticle formulations produced ALP activities significantly higher than the basal control ($p < 0.05$) and comparable to the osteogenic-medium control, whereas exposure to the particles themselves resulted in only a modest increase. These findings suggest that the sustained release of Ca^{2+} and Sr^{2+} ions from dissolving BGNPs is the main factor promoting osteogenic differentiation, with intact nanoparticles playing a minimal role until significant dissolution occurs.

The radical scavenging capability of both CS-BGNPs and SP-BGNPs was evaluated by the fluorescent spectroscopy analysis of the DCF signal produced by the oxidation of DCFDA after treatment with TBHP. As expected, the relative fluorescent units (RFU) of the control samples for all media (basal, osteogenic, SP-BGNPs and CS-BGNPs) increased when the TBHP was added (Figure 8b), given that TBHP is an oxidising agent. Each sample was found to be statistically different from its respective control with 99% confidence, indicating that the added TBHP successfully created an oxidizing environment, allowing for an accurate assessment of the BGNPs' effects. Additionally, the basal, osteogenic, SP-BGNPs and CS-BGNPs samples were compared to each other to understand the different effects of each media when exposed to oxidising conditions. The basal TBHP sample was found to be statistically different to the other three TBHP samples. However, no statistical difference was found between osteogenic, SP-BGNPs and CS-

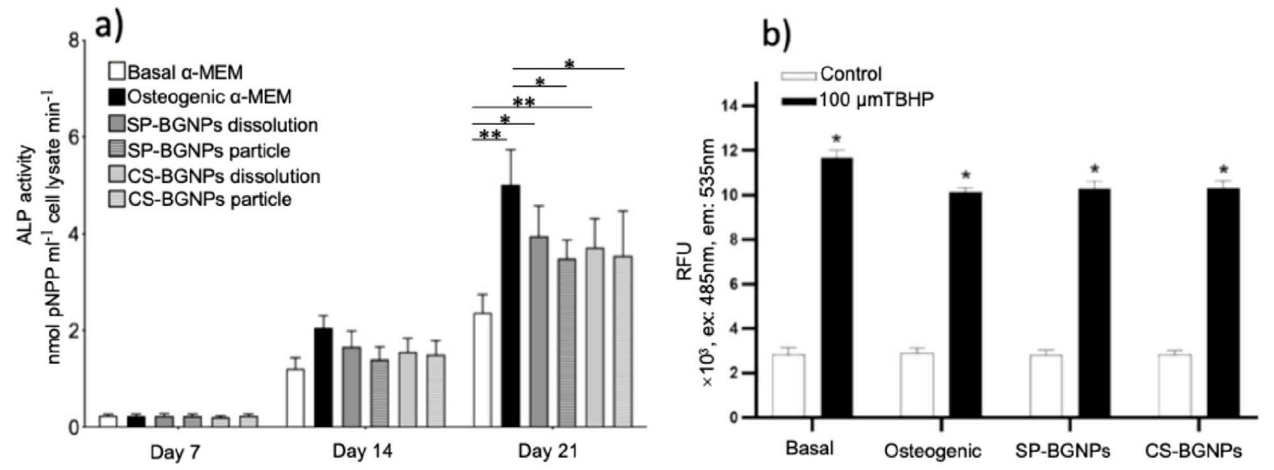

FIGURE 8
(a) ALP activity of MC3T3-E1 cells treated with 0.1 µg mL^{-1} of CS-BGNPs and SP-BGNPs over 3 weeks (7, 14 and 21 days), compared to cells cultured under the basal media control and osteogenic media, $p < 0.05$, (n = 3). **(b)** Radical scavenger capability of CS-BGNPs and SP-BGNPs (0.1 µg mL^{-1}) in MC3T3-E1 cells treated with the oxidising agent t-butyl hydroperoxide (TBHP): Bar intensity (relative fluorescence units RFU) represents the ROS fluorescence of media (black bars are for media containing TBHP (basal media, osteogenic media and media containing CS-BGNPs and SP-BGNPs); white bars are controls (the same media without TBHP); for the black bars, lower intensity represents the higher radical scavenger property. * = 99% confidence ($p < 0.05$) statistical significance against respective controls. ** = 99% confidence ($p < 0.01$) statistical significance against respective controls.

BGNPs media. The RFU signal obtained from the basal media sample was significantly higher than the osteogenic, SP-BGNPs and CS-BGNPs samples, suggesting that the BGNPs have a better radical scavenging capability than the basal media. In addition, the osteogenic media has a similar scavenging capability than the BGNPs because no statistical difference was found which suggests that the antioxidant properties of the nanoparticles are ideal to create an osteogenic environment.

Elevated levels of reactive oxygen species (ROS) serve as indicators of oxidative stress in cellular components like mitochondria, potentially leading to impaired cellular function and disrupted osteogenesis (Alcaide et al., 2010; Roesslein et al., 2013). However, at lower ROS levels, cells can activate protective mechanisms to manage and mitigate the oxidative challenge. Alcaide et al. studied the radical scavenging ability of pristine BGNPs when cultured with Saos-2 osteoblasts and L929 fibroblasts. No significant differences were found between the control (DMEM) and three different time points (3 h, 3 days and 7 days) of samples of BGNPs used (Alcaide et al., 2010). The study used ordered mesoporous $85SiO_2–10CaO–5P_2O_5$ (mol%) bioactive glass (S85 m, MBG85). In contrast, in the radical scavenging experiment reported here, a positive statistical difference was measured between the basal media and the BGNPs used (SP-BGNPs and CS-BGNPs). This effect can be attributed to the Sr ions' antioxidant capability, which can produce optimal osteoblastic differentiation of MC3T3-E1 cells (Pinna et al., 2021).

Conclusion

Bioinspired BGNPs with tunable size and morphology were synthesized via a one-pot modified Stöber process using either pure water or an ethanol/water mixture. This method effectively incorporated Sr^{2+} and Ca^{2+} ions while maintaining a predominantly amorphous and highly connected silicate network, ensuring the particles retain the osteogenic activity associated with Ca and Sr ion release. Two distinct morphologies, spherical and core-shell-like, were achieved by simply introducing ethanol as a co-solvent during synthesis.

MC3T3-E1 cell viability was not significantly affected by CS-BGNPs at concentrations up to 0.1 µg mL^{-1}, whereas SP-BGNPs exhibited low toxicity even at concentrations up to 10 µg mL^{-1} after 72 h of treatment. This demonstrates that nanoparticle size influences cytotoxicity, with smaller SP-BGNPs exhibiting reduced cytotoxicity relative to larger CS-BGNPs. The observed differences in toxicity are attributed to variations in nanoparticle morphology, which affect silica degradation rates and ion release profiles in cell culture media.

The presence of Ca^{2+} and Sr^{2+} ions in BGNPs enhanced pre-osteoblast activity. Furthermore, Sr^{2+} doping imparted antioxidant properties by scavenging reactive oxygen species, thus offering a dual therapeutic effect, promoting osteogenesis while mitigating oxidative stress known to impair bone formation.

Collectively, these findings highlight the potential of morphologically tailored, ion-doped BGNPs as versatile platforms for next-generation osteoporosis therapies. Future investigations should focus on *in vivo* efficacy and exploiting core-shell-like architectures for controlled delivery of bioactive agents to further enhance therapeutic outcomes.

Data availability statement

The raw data supporting the conclusions of this article will be made available by the authors, without undue reservation.

Author contributions

JP: Data curation, Conceptualization, Writing – original draft. AM: Writing – original draft, Formal Analysis. SA: Data curation, Writing – review and editing. SL: Data curation, Methodology, Formal Analysis, Writing – original draft, Investigation. SE: Data curation, Formal Analysis, Software, Conceptualization, Investigation, Writing – original draft. NK: Formal Analysis, Investigation, Writing – review and editing, Methodology. DB: Data curation, Formal Analysis, Writing – review and editing. GK: Formal Analysis, Data curation, Writing – review and editing, Methodology, Investigation, Software. AP: Writing – review and editing. JH: Writing – review and editing, Validation. JJ: Validation, Writing – review and editing. AP: Writing – original draft, Formal Analysis, Funding acquisition, Visualization, Conceptualization, Resources, Project administration, Methodology, Supervision, Writing – review and editing, Investigation, Validation, Data curation.

Funding

The author(s) declare that financial support was received for the research and/or publication of this article. The research work has received funding by the Marie Sklodowska-Curie Actions (MSCA) Individual fellowship (IF) in Horizon 2020 program of the European Union and Imperial college research fellowship (ICRF). JVH acknowledges financial support for the solid-state NMR instrumentation at Warwick used in this research which was funded by the EPSRC (grants EP/M028186/1 and EP/K024418/1), the University of Warwick, and the Birmingham Science City AM1 and AM2 projects which were supported by Advantage West Midlands (AWM) and the European Regional Development Fund (ERDF).

Conflict of interest

Author SL was employed by Visiting Specialist Services Academy Ltd.

The remaining authors declare that the research was conducted in the absence of any commercial or financial relationships that could be construed as a potential conflict of interest.

Generative AI statement

The author(s) declare that no Generative AI was used in the creation of this manuscript.

Any alternative text (alt text) provided alongside figures in this article has been generated by Frontiers with the support of artificial intelligence and reasonable efforts have been made to ensure accuracy, including review by the authors wherever possible. If you identify any issues, please contact us.

Publisher's note

Supplementary material

The Supplementary Material for this article can be found online at: https://www.frontiersin.org/articles/10.3389/fnano.2025.1634210/full#supplementary-material

References

Aghajanpour, S., Esfandyari-Manesh, M., Ghahri, T., Ghahremani, M. H., Atyabi, F., Heydari, M., et al. (2022). Impact of oxygen-calcium-generating and bone morphogenetic protein-2 nanoparticles on survival and differentiation of bone marrow-derived mesenchymal stem cells in the 3D bio-printed scaffold. *Colloids Surfaces B Biointerfaces* 216, 112581. doi:10.1016/j.colsurfb.2022.112581

Al Zadjali, F., Brooks, J., O'Neill, T. W., and Stanmore, E. (2024). Experiences of postmenopausal osteoporosis: a narrative review. *Disabil. Rehabilitation* 46 (5), 828–840. doi:10.1080/09638288.2023.2169770

Alcaide, M., Portolés, P., López-Noriega, A., Arcos, D., Vallet-Regí, M., and Portolés, M. (2010). Interaction of an ordered mesoporous bioactive glass with osteoblasts, fibroblasts and lymphocytes, demonstrating its biocompatibility as a potential bone graft material. *Acta Biomater.* 6 (3), 892–899. doi:10.1016/j.actbio.2009.09.008

Antoniac, I. V. (2016). *Handbook of bioceramics and biocomposites*. Germany: Springer Berlin.

Aveline, P., Cesaro, A., Mazor, M., Best, T. M., Lespessailles, E., and Toumi, H. (2021). Cumulative effects of strontium ranelate and impact exercise on bone mass in ovariectomized rats. *Int. J. Mol. Sci.* 22 (6), 3040. doi:10.3390/ijms22063040

Barrioni, B. R., de Carvalho, S. M., Naruphontjirakul, P., Norris, E., Kelly, N. L., Hanna, J. V., et al. (2022). Cobalt-containing spherical glass nanoparticles for therapeutic ion release. *J. Am. Ceram. Soc.* 105 (3), 1765–1777. doi:10.1111/jace.17916

Boyd, A. R., Rutledge, L., Randolph, L., and Meenan, B. (2015). Strontium-substituted hydroxyapatite coatings deposited *via* a co-deposition sputter technique. *Mater. Sci. Eng. C* 46, 290–300. doi:10.1016/j.msec.2014.10.046

Brinker, C. J., and Scherer, G. W. (1990). "The physics and chemistry of sol–gel processing," in *Sol-gel science*, 3. Academic Press.

Celik, B., Leal, A. F., and Tomatsu, S. (2024). Potential targeting mechanisms for bone-directed therapies. *Int. J. Mol. Sci.* 25 (15), 8339. doi:10.3390/ijms25158339

Chandran, M., Akesson, K. E., Javaid, M. K., Harvey, N., Blank, R. D., Brandi, M. L., et al. (2024). Impact of osteoporosis and osteoporosis medications on fracture healing: a narrative review. *Osteoporos. Int.* 35 (8), 1337–1358. doi:10.1007/s00198-024-07059-8

Chen, Q., Ge, Y., Granbohm, H., and Hannula, S. P. (2018). Effect of ethanol on ag@ Mesoporous silica formation by *in situ* modified stöber method. *Nanomaterials* 8 (6), 362. doi:10.3390/nano8060362

Choe, Y.-E., Kim, Y. J., Jeon, S. J., Ahn, J. Y., Park, J. H., Dashnyam, K., et al. (2022). Investigating the mechanophysical and biological characteristics of therapeutic dental cement incorporating copper doped bioglass nanoparticles. *Dent. Mater.* 38 (2), 363–375. doi:10.1016/j.dental.2021.12.019

Clogston, J. D., and Patri, A. K. (2010). "Zeta potential measurement," in *Characterization of nanoparticles intended for drug delivery*. Springer, 63–70.

Corenblit, D., Baas, A. C., Bornette, G., Darrozes, J., Delmotte, S., Francis, R. A., et al. (2011). Feedbacks between geomorphology and biota controlling Earth surface processes and landforms: a review of foundation concepts and current understandings. *Earth-Science Rev.* 106 (3-4), 307–331. doi:10.1016/j.earscirev.2011.03.002

Dalby, K. N., Nesbitt, H. W., Zakaznova-Herzog, V. P., and King, P. L. (2007). Resolution of bridging oxygen signals from O 1s spectra of silicate glasses using XPS: implications for O and Si speciation. *Geochimica Cosmochimica Acta* 71 (17), 4297–4313. doi:10.1016/j.gca.2007.07.005

De Villiers, J. P. (1971). Crystal structures of aragonite, strontianite, and witherite. *Am. Mineralogist J. Earth Planet. Mater.* 56 (5-6), 758–767. Available online at: https://rruff.geo.arizona.edu/doclib/am/vol56/AM56_758.pdf?utm_source=chatgpt.com.

Diba, M., Camargo, W. A., Brindisi, M., Farbod, K., Klymov, A., Schmidt, S., et al. (2017). Composite colloidal gels made of bisphosphonate-functionalized gelatin and bioactive glass particles for regeneration of osteoporotic bone defects. *Adv. Funct. Mater.* 27 (45), 1703438. doi:10.1002/adfm.201703438

Downs, R. T., and Hall-Wallace, M. (2003). The American mineralogist crystal structure database. *Am. mineralogist* 88 (1), 247–250. Available online at: https://www.geo.arizona.edu/xtal/group/pdf/am88_247.pdf.

Fischer, V., and Haffner-Luntzer, M. (2022). "Interaction between bone and immune cells: implications for postmenopausal osteoporosis," in *Seminars in cell and developmental biology*. Elsevier.

Foroutan, F., Abrahams, I., Smales, G. J., Kanwal, N., di Pasquale, R., Knowles, J. C., et al. (2024). A sol-gel templating route for the synthesis of hierarchical porous calcium phosphate glasses containing zinc. *Ceram. Int.* 50 (20), 38174–38182. doi:10.1016/j.ceramint.2024.07.180

Fuggle, N. R., Beaudart, C., Bruyère, O., Abrahamsen, B., Al-Daghri, N., Burlet, N., et al. (2024). Evidence-based guideline for the management of osteoporosis in men. *Nat. Rev. Rheumatol.* 20 (4), 241–251. doi:10.1038/s41584-024-01094-9

García-Perdiguero, J. C., Gómez-Cerezo, N., Gisbert-Garzarán, M., Manzano, M., and Vallet-Regí, M. (2025). Unraveling the role of calcium in the osteogenic behavior of mesoporous bioactive glass nanoparticles. *Acta Biomater.*

Gentleman, E., Fredholm, Y. C., Jell, G., Lotfibakhshaiesh, N., O'Donnell, M. D., Hill, R. G., et al. (2010). The effects of strontium-substituted bioactive glasses on osteoblasts and osteoclasts *in vitro*. *Biomaterials* 31 (14), 3949–3956. doi:10.1016/j.biomaterials.2010.01.121

Ghahri, T., Salehi, Z., Aghajanpour, S., Eslaminejad, M. B., Kalantari, N., Akrami, M., et al. (2023). Development of osteon-like scaffold-cell construct by quadruple coaxial extrusion-based 3D bioprinting of nanocomposite hydrogel. *Biomater. Adv.* 145, 213254. doi:10.1016/j.bioadv.2022.213254

Gritsch, L., Perrin, E., Chenal, J. M., Fredholm, Y., Maçon, A. L., Chevalier, J., et al. (2021). Combining bioresorbable polyesters and bioactive glasses: orthopedic applications of composite implants and bone tissue engineering scaffolds. *Appl. Mater. Today* 22, 100923. doi:10.1016/j.apmt.2020.100923

Harris, R. K., Becker, E. D., Cabral de Menezes, S. M., Goodfellow, R., and Granger, P. (2002). NMR nomenclature: nuclear spin properties and conventions for chemical shifts. IUPAC recommendations 2001. International union of pure and applied chemistry. Physical chemistry division. Commission on molecular structure and spectroscopy. *Magnetic Reson. Chem.* 40 (7), 489–505. doi:10.1002/mrc.1042

Hembury, M., Chiappini, C., Bertazzo, S., Kalber, T. L., Drisko, G. L., Ogunlade, O., et al. (2015). Gold–silica quantum rattles for multimodal imaging and therapy. *Proc. Natl. Acad. Sci.* 112 (7), 1959–1964. doi:10.1073/pnas.1419622112

Hesaraki, S., Nouri-Felekori, M., Nezafati, N., and Borhan, S. (2021). Preparation, characterization, and *in vitro* biological performance of novel porous GPTMS-Coupled tragacanth/nano-bioactive glass bone tissue scaffolds. *Mater. Today Commun.* 27, 102335. doi:10.1016/j.mtcomm.2021.102335

Hoppe, A., Güldal, N. S., and Boccaccini, A. R. (2011). A review of the biological response to ionic dissolution products from bioactive glasses and glass-ceramics. *Biomaterials* 32 (11), 2757–2774. doi:10.1016/j.biomaterials.2011.01.004

Huang, Y.-R., and Ding, S.-J. (2025). Exploring processing–structure–property relationships of chemically precipitated strontium silicate particles for medical applications. *J. Mater. Chem. B* 13 (12), 3990–4005. doi:10.1039/d4tb02656j

Hurt, A., Getti, G., and Coleman, N. (2014). Bioactivity and biocompatibility of a chitosan-tobermorite composite membrane for guided tissue regeneration. *Int. J. Biol. Macromol.* 64, 11–16. doi:10.1016/j.ijbiomac.2013.11.020

Islam, M. T., Felfel, R. M., Abou Neel, E. A., Grant, D. M., Ahmed, I., and Hossain, K. M. Z. (2017). Bioactive calcium phosphate–based glasses and ceramics and their biomedical applications: a review. *J. tissue Eng.* 8, 2041731417719170. doi:10.1177/2041731417719170

Jacobsen, V., Kunisch, E., Merle, C., Xue, B., Zheng, K., Renkawitz, T., et al. (2025). Cerium-doped mesoporous bioactive glass nanoparticles reduce oxidative stress and adipogenic differentiation in human bone marrow-derived mesenchymal stromal cells. *J. Trace Elem. Med. Biol.* 88, 127617. doi:10.1016/j.jtemb.2025.127617

Jelin-Uhlig, S., Weigel, M., Ott, B., Imirzalioglu, C., Howaldt, H. P., Böttger, S., et al. (2024). Bisphosphonate-related osteonecrosis of the jaw and oral microbiome: clinical risk factors, pathophysiology and treatment options. *Int. J. Mol. Sci.* 25 (15), 8053. doi:10.3390/ijms25158053

Khamsehashari, N., Hassanzadeh-Tabrizi, S., and Bigham, A. (2018). Effects of strontium adding on the drug delivery behavior of silica nanoparticles synthesized by P123-assisted sol-gel method. *Mater. Chem. Phys.* 205, 283–291. doi:10.1016/j.matchemphys.2017.11.034

Khodaee, P., Najmoddi, N., and Shahrad, S. (2018). "The effect of ethanol and temperature on the structural properties of mesoporous silica synthesized by the sol-gel method," in *2018 25th national and 3rd international iranian conference on biomedical engineering (ICBME)*. IEEE.

Kim, M.-K., Lee, H. N., Jenjob, R., Lee, J., and Yang, S. G. (2017). Calcium-triggered pulsatile delivery of parathyroid hormone from microbeads for osteoporosis treatment. *Biomacromolecules* 18 (10), 3099–3105. doi:10.1021/acs.biomac.7b00750

Kourkoumelis, N. (2016). Osteoporosis and strontium-substituted hydroxyapatites. *Ann. Transl. Med.* 4 (Suppl. 1), S10. doi:10.21037/atm.2016.10.03

Lee, J.-H., Mandakhbayar, N., El-Fiqi, A., and Kim, H. W. (2017). Intracellular co-delivery of Sr ion and phenamil drug through mesoporous bioglass nanocarriers synergizes BMP signaling and tissue mineralization. *Acta Biomater.* 60, 93–108. doi:10.1016/j.actbio.2017.07.021

Li, Z. H., Gong, Y. J., Wu, D., Sun, Y. H., Wang, J., Liu, Y., et al. (2001). SAXS analysis of interface in organo-modified mesoporous silica. *Surf. Interface Analysis An Int. J. devoted Dev. Appl. Tech. analysis surfaces, interfaces thin films* 31 (9), 897–900. doi:10.1002/sia.1118

Li, Y., Bastakoti, B. P., and Yamauchi, Y. (2015). Smart soft-templating synthesis of hollow mesoporous bioactive glass spheres. *Chemistry–A Eur. J.* 21 (22), 8038–8042. doi:10.1002/chem.201406570

Maçon, A. L., Lee, S., Poologasundarampillai, G., Kasuga, T., and Jones, J. R. (2017). Synthesis and dissolution behaviour of CaO/srO-Containing sol–gel-derived 58S glasses. *J. Mater. Sci.* 52, 8858–8870. doi:10.1007/s10853-017-0869-0

Malhotra, A., and Habibovic, P. (2016). Calcium phosphates and angiogenesis: implications and advances for bone regeneration. *Trends Biotechnol.* 34 (12), 983–992. doi:10.1016/j.tibtech.2016.07.005

Meskher, H., Sharifianjazi, F., Tavamaishvili, K., Irandoost, M., Nejadkoorki, D., and Makvandi, P. (2024). Limitations, challenges and prospective solutions for bioactive glasses-based nanocomposites for dental applications: a critical review. *J. Dent.* 150, 105331. doi:10.1016/j.jdent.2024.105331

Moghaddam, Z., Nery, E. T., Unalan, I., Hoxha, A., Felipe-Sotelo, M., Zhao, H., et al. (2025). Electrospun porous phosphate-based glass fibres containing gallium and clove oil: cytotoxicity and antioxidant properties. *Ceram. Int.* 51, 23279–23288. doi:10.1016/j.ceramint.2025.03.017

Naruphontjirakul, P., Greasley, S. L., Chen, S., Porter, A. E., and Jones, J. R. (2016). Monodispersed strontium containing bioactive glass nanoparticles and MC3T3-E1 cellular response. *Biomed. Glas.* 2 (1). doi:10.1515/bglass-2016-0009

Naruphontjirakul, P., Porter, A. E., and Jones, J. R. (2018). *In vitro* osteogenesis by intracellular uptake of strontium containing bioactive glass nanoparticles. *Acta Biomater.* 66, 67–80. doi:10.1016/j.actbio.2017.11.008

Naruphontjirakul, P., Li, S., Pinna, A., Barrak, F., Chen, S., Redpath, A. N., et al. (2022). Interaction of monodispersed strontium containing bioactive glass nanoparticles with macrophages. *Biomater. Adv.* 133, 112610. doi:10.1016/j.msec.2021.112610

Nesbitt, H., Bancroft, G., Henderson, G., Ho, R., Dalby, K., Huang, Y., et al. (2011). Bridging, non-bridging and free (O2−) oxygen in Na2O-SiO2 glasses: an X-ray photoelectron spectroscopic (XPS) and nuclear magnetic resonance (NMR) study. *J. non-crystalline solids* 357 (1), 170–180. doi:10.1016/j.jnoncrysol.2010.09.031

Orcel, G., Hench, L., Artaki, I., Jonas, J., and Zerda, T. (1988). Effect of formamide additive on the chemistry of silica sol-gels II. Gel structure. *J. non-crystalline solids* 105 (3), 223–231. doi:10.1016/0022-3093(88)90311-0

Ou, J., Wang, T., Lei, R., Sun, M., Ruan, X., Wei, J., et al. (2025). Association between cardiovascular health and osteoporotic fractures: a national population-based study. *Sci. Rep.* 15 (1), 3844. doi:10.1038/s41598-025-88020-5

Pierre, L., Ito, A., and Tateishi, T. (2005). Sol-gel synthesis of amorphous calcium phosphate and sintering into microporous hydroxyapatite bioceramics. *J. Am. Ceram. Soc.* 81 (6), 1421–1428. doi:10.1111/j.1151-2916.1998.tb02499.x

Pinna, A., Torki Baghbaderani, M., Vigil Hernández, V., Naruphontjirakul, P., Li, S., McFarlane, T., et al. (2021). Nanoceria provides antioxidant and osteogenic properties to mesoporous silica nanoparticles for osteoporosis treatment. *Acta Biomater.* 122, 365–376. doi:10.1016/j.actbio.2020.12.029

Polo-Montalvo, A., Casarrubios, L., Serrano, M. C., Sanvicente, A., Feito, M. J., Arcos, D., et al. (2021). Effective actions of ion release from mesoporous bioactive glass and macrophage mediators on the differentiation of osteoprogenitor and endothelial progenitor cells. *Pharmaceutics* 13 (8), 1152. doi:10.3390/pharmaceutics13081152

Porod, G. (1951). Die Röntgenkleinwinkelstreuung von dichtgepackten kolloiden systemen: I. Teil. *Kolloid-Zeitschrift* 124 (2), 83–114. doi:10.1007/bf01512792

Queiroz, P. M., Barrioni, B. R., Valverde, T. M., de Goes, A. M., Gomes, D. A., and Pereira, M. d. M. (2023). Study of the manganese and calcium synergetic influence on mesoporous bioactive glass characteristic. *J. non-crystalline solids* 622, 122656. doi:10.1016/j.jnoncrysol.2023.122656

Rice, S. A. (1956). "Small angle scattering of x-rays. A guinier and G fournet translated by CB wilson and with a bibliographical appendix by KL yudowitch,", 1955. New York: Wiley, 268.

Rodriguez-Loya, J., Lerma, M., and Gardea-Torresdey, J. L. (2023). Dynamic light scattering and its application to control nanoparticle aggregation in colloidal systems: a review. *Micromachines* 15 (1), 24. doi:10.3390/mi15010024

Roesslein, M., Hirsch, C., Kaiser, J. P., Krug, H., and Wick, P. (2013). Comparability of *in vitro* tests for bioactive nanoparticles: a common assay to detect reactive oxygen species as an example. *Int. J. Mol. Sci.* 14 (12), 24320–24337. doi:10.3390/ijms141224320

Ruiz-Clavijo, A., Hurt, A. P., Kotha, A. K., and Coleman, N. J. (2019). Effect of calcium precursor on the bioactivity and biocompatibility of sol-gel-derived glasses. *J. Funct. Biomaterials* 10 (1), 13. doi:10.3390/jfb10010013

Saha, A., Narula, K., Mishra, P., Biswas, G., and Bhakta, S. (2023). A facile cost-effective electrolyte-assisted approach and comparative study towards the greener synthesis of silica nanoparticles. *Nanoscale Adv.* 5, 1386–1396. doi:10.1039/d2na00872f

Sakurai, R., Takeuchi, I., Makino, K., Itoh, F., and Saitoh, A. (2024). Usefulness of percutaneous estradiol-loaded PLGA-PEG-PLGA nanoparticles for the treatment of osteoporosis. *Results Mater.* 22, 100577. doi:10.1016/j.rinma.2024.100577

Schindelin, J., Arganda-Carreras, I., Frise, E., Kaynig, V., Longair, M., Pietzsch, T., et al. (2012). Fiji: an open-source platform for biological-image analysis. *Nat. methods* 9 (7), 676–682. doi:10.1038/nmeth.2019

Schumacher, M., Habibovic, P., and van Rijt, S. (2021). Mesoporous bioactive glass composition effects on degradation and bioactivity. *Bioact. Mater.* 6 (7), 1921–1931. doi:10.1016/j.bioactmat.2020.12.007

Shafiu Kamba, A., and Zakaria, Z. A. B. (2014). Osteoblasts growth behaviour on bio-based calcium carbonate aragonite nanocrystal. *BioMed Res. Int.* 2014 (1), 1–9. doi:10.1155/2014/215097

Shishkina, E., Shuiskaya, A., and Sharagin, P. (2023). Bone marrow dosimetry for mice: exposure from bone-seeking 89, 90Sr. *Radiat. Environ. Biophysics* 62 (1), 131–142. doi:10.1007/s00411-022-01010-3

Siekkinen, M. (2024). “The impact of dissolution products and solution pH on *in vitro* behaviour of the bioactive glasses 45S5 and S53P4.”

Talib, S. M., Haider, A. J., Al-Musawi, S., Al-Joudi, F. S., and Ahmed, S. A. (2025). Laser-fabricated metal oxide core–shell nanoparticles for biomedical applications: a mini review. *Plasmonics*, 1–18. doi:10.1007/s11468-024-02469-0

Thanasrisuebwong, P., Jones, J. R., Eiamboonsert, S., Ruangsawasdi, N., Jirajariyavej, B., and Naruphontjirakul, P. (2022). Zinc-containing sol–gel glass nanoparticles to deliver therapeutic ions. *Nanomaterials* 12 (10), 1691. doi:10.3390/nano12101691

Thommes, M., Kaneko, K., Neimark, A. V., Olivier, J. P., Rodriguez-Reinoso, F., Rouquerol, J., et al. (2015). Physisorption of gases, with special reference to the evaluation of surface area and pore size distribution (IUPAC technical report). *Pure Appl. Chem.* 87 (9-10), 1051–1069. doi:10.1515/pac-2014-1117

Toufiq, A. M., Wang, F., Javed, Q. u. a., and Li, Y. (2013). Influence of SiO2 on the structure-controlled synthesis and magnetic properties of prismatic MnO2 nanorods. *Nanotechnology* 24 (41), 415703. doi:10.1088/0957-4484/24/41/415703

Tovani, C. B., Oliveira, T. M., Gloter, A., and Ramos, A. P. (2018). Sr2+-substituted CaCO3 nanorods: impact on the structure and bioactivity. *Cryst. Growth and Des.* 18 (5), 2932–2940. doi:10.1021/acs.cgd.8b00017

Tu, K. N., Lie, J. D., Wan, C. K. V., Cameron, M., Austel, A. G., Nguyen, J. K., et al. (2018). Osteoporosis: a review of treatment options. *Pharm. Ther.* 43 (2), 92–104.

Xuan, M., Wang, B., Bi, W., Li, Y., Song, L., Xie, Z., et al. (2025). Treatment of postmenopausal osteoporosis with recombinant human parathyroid hormone and electromagnetic field. *Aging Clin. Exp. Res.* 37 (1), 44–46. doi:10.1007/s40520-025-02932-w

Yao, Y., Cai, X., Chen, Y., Zhang, M., and Zheng, C. (2025). Estrogen deficiency-mediated osteoimmunity in postmenopausal osteoporosis. *Med. Res. Rev.* 45 (2), 561–575. doi:10.1002/med.22081

You, J., Zhang, Y., and Zhou, Y. (2022). Strontium functionalized in biomaterials for bone tissue engineering: a prominent role in osteoimmunomodulation. *Front. Bioeng. Biotechnol.* 10, 928799. doi:10.3389/fbioe.2022.928799

Zadsirjan, S., Dehkordi, N. P., Heidari, S., Najafi, F., Zargar, N., Feli, M., et al. (2024). Synthesis of a calcium silicate cement containing a calcinated strontium silicate phase. *Int. J. Dent.* 2024 (1), 8875014. doi:10.1155/2024/8875014

Zeng, J., Guo, J., Sun, Z., Deng, F., Ning, C., and Xie, Y. (2020). Osteoblastic and anti-osteoclastic activities of strontium-substituted silicocarnotite ceramics: *in vitro* and *in vivo* studies. *Bioact. Mater.* 5 (3), 435–446. doi:10.1016/j.bioactmat.2020.03.008

Zhang, Y., Yu, J., Wu, C., Han, L., Tai, Y., Wang, B., et al. (2025). Electrophoretic deposition of curcumin-loaded mesoporous bioactive glass nanoparticle-chitosan composite coatings on titanium for treating tumor-induced bone defect. *Compos. Part B Eng.* 289, 111950. doi:10.1016/j.compositesb.2024.111950